THESIS FOR THE DEGREE OF LICENTIATE IN ENGINEERING

DNS and LES of Turbulent Natural Convection Boundary Layer

DARIOUSH G. BARHAGHI

Division of Thermo and Fluid Dynamics

CHALMERS UNIVERSITY OF TECHNOLOGY

Göteborg, Sweden, 2004

DNS and LES of Turbulent Natural Convection Boundary Layer

DARIOUSH G. BARHAGHI

ISSN 1101-9972
ISRN CTH-TFD-PB-04/05

Division of Thermo and Fluid Dynamics
Chalmers University of Technology
SE-412 96 Göteborg, Sweden
Phone: +46-(0)31-7721400
Fax: +46-(0)31-180976

Printed at Chalmers Reproservice
Göteborg, Sweden 2004

To the memory of my grandfather

DNS and LES of Turbulent Natural Convection Boundary Layer

by
Darioush G. Barhaghi
darioush@tfd.chalmers.se
Division of Thermo and Fluid Dynamics
Chalmers University of Technology
SE-412 96 Göteborg
Sweden

Abstract

Turbulent natural convection boundary layers possess some special characteristics compared to the other boundary layers. In order to study this kind of boundary layer, two powerful numerical methods, *Direct Numerical Simulation* or DNS and *Large Eddy Simulation* or LES, are used. The former is used to investigate the natural convection boundary layer in a vertical channel for which the Grashof number based on the channel width is $Gr_h = 9.6 \cdot 10^5$ and the latter is used to study the natural convection in a cylindrical vertical shell and tube. The local Grashof number in the latter case reaches $Gr_z = 5 \cdot 10^{11}$. Mean flow parameters as well as turbulence parameters in the both cases are studied and the results are compared with the existing experimental results for natural convection boundary layer on a flat plate and natural convection boundary layer on a vertical slender cylinder. Although many qualitative and quantitative agreements are found between the results, there are still some discrepancies in the turbulence characteristics. A region with negative shear stress in the boundary layer along the vertical cylinder, which is in agreement with many experiments is observed and the effect of it on the boundary layer is studied. However, there is no such region in the boundary layer inside the vertical channel. Also the existence of a linear region for the velocity profile which is much thinner than the ordinary forced convection boundary layers is confirmed.

Keywords: LES, DNS, natural convection boundary layer, free convection, vertical cylinder

Preface

Based on the Chapter 3, the paper: D. G. Barhaghi, L. Davidson and R. Karlsson, ”Large Eddy Simulation of Natural Convection Boundary Layer on a Vertical Cylinder” is prepared which will be presented at ”ERCOFTAC International Symposium on Engineering Turbulence Modelling and Measurements (ETMM6), Sardinia, Italy, 2005”.

Acknowledgments

This work was conducted at the Division of Thermo and Fluid Dynamics at Chalmers University of Technology.

I would like to express my sincere gratitudes to Professor Dr. Lars Davidson for his support and guidance throughout the course of this work. This thesis would never reach to this point without his enlightening discussions and brilliant advices.

I would like to thank Professor Dr. Rolf I. Karlsson and Dr. Shia-Hui Peng for sharing their ideas and knowledge.

I also would like to thank Monika Orrbacke, Sandra Arvidson and Ulla Lindberg-Thieme for their administrative support.

I am also grateful to all of my colleagues especially Niklas Andersson, Mattias Billson and Andreas Sveningsson for taking their time to fix my computer-related problems and Magnus Stridh for the wonderful time that we have had together.

Financial support from the Swedish Research Council and the computer resources which have been provided by the Center for Parallel Computing (PDC), KTH are greatly acknowledged.

My warmest and deepest sense of gratitude goes to my family especially my parents, Parisa and my family in Sweden for their unconditional support and understanding.

Nomenclature

$C_{\varepsilon 1}, C_{\varepsilon 2}$	turbulence model constants
C_k, C_μ	turbulence model constants
$C_\omega, C_{\omega 1}, C_{\omega 2}$	turbulence model constants
c_p	fluid specific heat at constant pressure
$\hat{e}_r$	unit vector in r-direction
$\hat{e}_z$	unit vector in z-direction
$f_\varepsilon, f_k, f_\mu$	turbulence model damping functions
g_r	gravitational acceleration in r-direction
g_z	gravitational acceleration in z-direction
H	height of the shell and tube and the cavity
h	convection heat transfer coefficient
k	turbulence kinetic energy; fluid thermal conductivity
n	normal distance from the wall
n^+	dimensionless normal distance from the wall, $v_n^* n/\nu$
P_k	turbulence production
Pr_t	turbulent Prandtl number, 0.9 for RANS models and 0.4 for LES
p	pressure
q_w	wall heat flux, $-k\partial T/\partial n$
R_i	hot tube (inner) radius
R_o	shell (outer) radius
r	distance in radial direction
Δr	radial cell width in cylindrical coordinate system
r_{max}	location of maximum velocity in the boundary layer
r^+	dimensionless distance from wall, $v_z^*(r - R_i)/\nu$
r_v	velocity boundary layer thickness (see section 2.4)
r_T	thermal boundary layer thickness (see section 2.4)
S	clockwise distance from southwest corner
t	time
t^*	friction temperature, $q_w/(\rho c_p v^*)$
$\overline{T}$	filtered temperature

T	temperature
T_c	cold wall temperature, the ambient temperature or the inlet temperature
T_f	film temperature, $(T_h[K] + T_c[K])/2$
T_h	hot wall temperature
T_{ref}	reference temperature, $(= T_c)$ in experimental rig and $(= T_f)$ in channel flow
T^+	dimensionless temperature, $(T_w - T)/t^*$
U_o	buoyant velocity, $\sqrt{g\beta(T_h - T_c)H}$
U_{bulk}	bulk velocity
v_{max}	maximum velocity in the boundary layer
v_n^*	friction velocity parallel to the wall, $\sqrt{\tau_w^n/\rho}$
$\overline{v_\theta}$	filtered velocity component in θ-direction
$\overline{v_r}$	filtered velocity component in r-direction
$\overline{v_z}$	filtered velocity component in z-direction
v_r	velocity component in r-direction
v_z	velocity component in z-direction
v_z^*	friction velocity, $\sqrt{\tau_w/\rho}$
v_z^+	dimensionless velocity, v_z/v_z^*
$\mathbf{V}$	velocity vector, $v_r\hat{e}_r + v_z\hat{e}_z$
$\Delta\mathcal{V}$	cell volume
w	vertical velocity in Cartesian coordinate system
W	width of the cavity
x	horizontal axis in Cartesian coordinate system
z	vertical axis in cylindrical and Cartesian coordinate system
Δz	cell length in cylindrical coordinate system
Δz^+	dimensionless cell length, $v_z^*\,\Delta z/\nu$

Greek Symbols

α	thermal diffusivity, $k/(\rho c_p)$
β	coefficient of expansion, $1/T_f[K]$
η	Kolmogrov length scale
ε	turbulence dissipation rate
κ	wave number
μ	fluid dynamic viscosity
ν_{eff}	effective kinematic viscosity
ν_t	turbulent kinematic viscosity

ω	specific dissipation, $\varepsilon/(0.09k)$
ρ	fluid density
$\sigma_\varepsilon, \sigma_k, \sigma_\omega$	turbulence Prandtl numbers
τ_w	wall shear stress, $\mu\partial v_z/\partial r$
τ_w^n	wall shear stress, $\mu\partial v_n/\partial n$
θ	azimuthal angle in cylindrical coordinate system
θ_t	dimensionless temperature, $(T - T_{ref})/(T_w - T_{ref})$
$\Delta\theta$	cell width in cylindrical coordinate system
$\Delta\theta^+$	dimensionless cell width, $\Delta\theta v_z^*/\nu$
ζ	dimensionless transverse coordinate, $r(\partial\theta_t/\partial r)_{r=R_i}$

Dimensionless quantities

C_f	friction coefficient, $\tau_w/(\rho U_o^2/2)$
Gr_z	local Grashof number, $g\beta(T_w - T_\infty)z^3/\nu^2$
Nu	Nusselt number, $-H(\partial T/\partial n)_w/(T_h - T_c)$
Nu_z	local Nusselt number, $-z(\partial T/\partial n)_w/(T_h - T_c)$
Pr	Prandtl number, ν/α
Ra_z	local Rayleigh number, $g\beta(T_w - T_\infty)z^3/(\nu\alpha)$

Subscript

c	cold
h	hot
w	wall
∞	ambient

Contents

Abstract **v**

Preface **vii**

Acknowledgments **ix**

Nomenclature **xi**

1 Introduction **1**

1.1 Heat Transfer 1

1.2 Natural Convection 2

1.3 Numerical Methods 3

1.3.1 RANS Methods 4

1.3.2 Large Eddy Simulation 5

1.3.3 Direct Numerical Simulation 7

1.4 Previous Investigations 7

1.5 Designing an LES Problem 12

1.6 Overview of the Present Study 14

2 RANS Modeling **15**

2.1 Governing Equations 15

2.2 Numerical Method 18
2.3 Turbulence Model Assessment 18
2.4 Effect of Inlet Velocity 20
2.5 Effect of Perforated Plate 24
2.6 Effect of Outlet Dimension 27
2.7 Effect of Inlet Dimension 28
2.8 Effect of Outer Shell Radius 28
2.9 Conclusions 31

3 Large Eddy Simulation **33**
3.1 Governing Equations 33
3.2 Computational Geometry 35
3.3 Numerical Method 35
3.4 Boundary Conditions 38
3.5 Fully Developed Flow Assessment 38
3.6 Grid and Domain Study 40
3.6.1 Grid Specifications 41
3.6.2 Computational Geometry Extension 42
3.7 Wiggle Detection 45
3.8 Mean Flow Quantities 45
3.9 Turbulence Quantities 51
3.10 Conclusions 55

4 Direct Numerical Simulation **57**
4.1 Governing equations 58
4.2 Numerical Method 59

4.3 Results 59

5 Discussions **67**

Bibliography **76**

A Energy Spectrum Calculation **83**

Chapter 1

Introduction

1.1 Heat Transfer

Heat transfer is an interesting scientific subject which has drawn scientists' attention to itself. Its importance continues to make it a major field of interest to engineers, designers and manufacturers. As this phenomenon exists in every aspect of the life, a better understanding of it can lead to benefits in humans life. The applications include not only industrial aspects like power generators, reactors, turbines, heat exchangers and other power conversion devices, but also natural aspects like atmospheric and oceanic currents, bio-heat transfer, green house effects and heat transfer in stellar atmospheres.

A consideration of the number of conferences which take place each year and published books, journals, articles and papers as well as awards which are bestowed to scientist who have had an important contribution to development of this science, reveals the importance of this subject. According to Goldstein *et al.* (2002) in year 2000, there have been at least 18 conferences and 24 published books about related aspects of heat transfer and its applications.

This science, is divided into three major fields: *Conduction, Convection and Radiation.* The methods of investigation of these subjects are also divided into three categories : *Numerical, Analytical and Experimental.* Any problem which consist of a way or combination of different ways of heat transfer, can usually be studied by any combination of these investigating methods.

The major concern of this study is the *Natural Convection Heat Trans-*

fer and approaching method to the problem is *Numerical method*.

1.2 Natural Convection

Regarding the convective heat transfer, this phenomenon is divided into two major categories, *Forced Convection* and *Natural* or *Free Convection*. Forced convection heat transfer, is a process in which the heat transfer among different phases or states, occurs because of velocity and temperature differences among them. It is primarily a kind of molecular diffusion which has been enhanced because of mixing process created due to already existing momentum difference. On the other hand, natural convection heat transfer takes place because of density differences in a liquid or gas phase. The density difference which is mostly caused by the temperature difference, along with the gravitational force, creates a so called buoyancy force which consequently creates a momentum difference. However, it should be mentioned that not every temperature gradient causes movement in the fluid. In fact, temperature difference should be in a way that provokes instability in the fluid. It is conventional to use *unstable* temperature difference to emphasize this difference. This is shown in Figure 1.1.

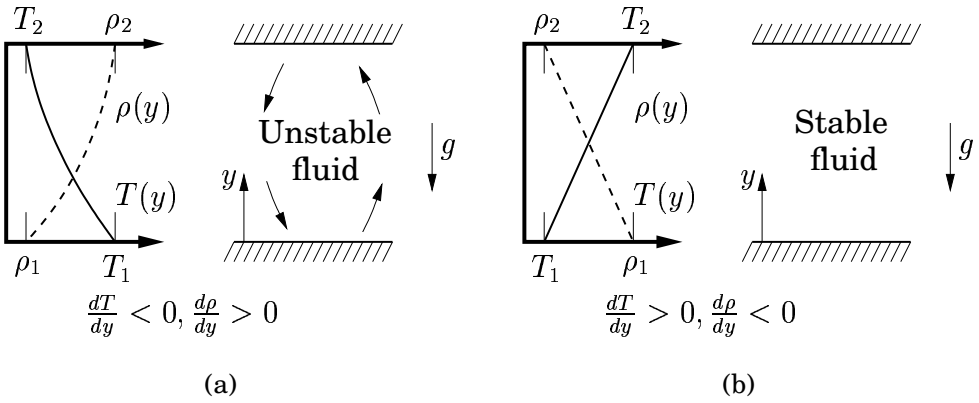

Figure 1.1: Unstable and stable fluid between two differentially heated horizontal walls.

Every convecting system is characterized by one or a blend of the two heat transfer processes, i.e. forced and natural convection. Basically all forced convection heat transfer processes comprise natural convection as well but due to small contribution compared to forced convection counterpart, natural convection is sometimes neglected. The impor-

tance of natural convection and its contribution to the heat transfer has also been studied in this work.

Usually, Nusselt number is considered in the form of $Nu_L = f(Re_L, Gr_L, Pr)$, where L is a characteristic length. When the inequality $(Gr_L/Re_L^2) \ll 1$ is satisfied, free convection effects may be neglected. Conversely, when $(Gr_L/Re_L^2) \gg 1$, forced convection effects may be neglected and in case of $(Gr_L/Re_L^2) \approx 1$ a combined effect of free and forced convection must be considered.

The number of heat transfer applications in which the natural convection is a dominant phenomenon are large and by studying it, new mysteries are continuously being discovered. Better understanding of this phenomenon has even increased the number of applications and has led to a number of sophisticated industrial and environmental designs. Whenever running costs are important or small efficiency improvements are vital and can play a vital role in energy consumption, this type of heat transfer is bound to come under scrutiny. Oceanographic and atmospheric problems such as green house effects, gulf stream and extreme climate changes, design of electrical and electronic devices, home appliances such as fridges and refrigerators, cooling towers, safety of reactors, economic conversion of saline to fresh water and direct contact exchangers are all problems that recently, have given a particular concern to this science.

1.3 Numerical Methods

In the engineering world, there are problems that can be explained by so called governing mathematical equations. Many of these equations are impossible to solve without simplifying assumptions. These assumptions cause generation of error in the results, which leads to descripancies between real world and theories. For so many years, experimental studies were the only reliable methods for investigating engineering problems. The advent of computers and their rapid advancement brought an opportunity to the scientists to analyze those problems with less simplifying assumptions. As the computers advanced more, lesser assumptions were made and more complicated problems were considered. The term *Numerical Method* is a very general term attributed to all of the methods which consist of estimating mathematical terms or equations numerically. In this text, however, it is referred to those methods which are to be used to solve the so called conser-

vation equations. These equations are mass, momentum or Navier-Stokes and energy equations. In many texts, the term Computational Fluid Dynamics or CFD is used instead, which is a more specific explanation of numerically solving of the conservation equations.

The conservation equations are a system of nonlinear partial differential equations for which, so far, no general mathematical solution has been proposed. In order to numerically solve these equations, they should be discretized and solved by an iterative method.

As long as the flow is laminar, the only problem is to solve this system of discretized equations. The accuracy of results depends on both the grid and the discretization scheme. Examples of these schemes are first order upwind, second order hybrid, power low and third order QUICK scheme (Versteegh & Malalasekera, 1995).

The moment that the flow becomes turbulent, a chaotic, random motion is observable. In this case, the instantaneous flow values at a fixed location in the flow show a fluctuating behavior. Turbulence, inherently, is a three dimensional, time dependent phenomenon. So, In order to study it numerically, different approaches have been proposed that have different accuracies which sometimes are flow dependent. The three major approaches are *Reynolds Averaged Navier-Stokes or RANS*, *Large Eddy Simulation or LES* and *Direct Numerical Simulation or DNS*. Considerable effort has been devoted to develop these methods in the recent decades and a important advancements have been achieved.

1.3.1 RANS Methods

Study of stationary turbulent flows, has shown that fluctuating flow quantities have a constant mean value (see e.g. Figure 1.2).

This fact, inspired Reynolds to decompose the dependent variables into an average and a fluctuating part and take the time integral average of the equations. Doing so, introduced new unknown parameters which are called Reynolds stresses. No longer the system of equations can be considered closed. This problem is referred to as turbulence closure problem which means that the number of unknown parameters are more than the number of equations.

RANS methods consist of those models which try to estimate these stresses which are representative of turbulent diffusion, by analogy

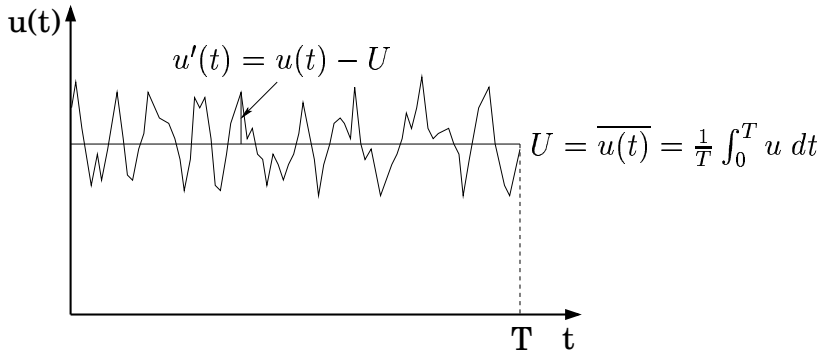

Figure 1.2: Typical point velocity measurements in turbulent flow.

to the molecular diffusion. This analogy is referred to as Boussinesq approximation which reads:

$$-\rho\overline{u_i' u_j'} = \mu_t \left(\frac{\partial U_i}{\partial x_j} + \frac{\partial U_j}{\partial x_i}\right) - \frac{1}{3}\overline{u_k' u_k'}\delta_{ij} \tag{1.1}$$

The drawback with these models is that they consider an isotropic turbulent viscosity. From experiments, it is known that this is often not the case. The accuracy limit of these models depends on the model length accuracy. This means that there is a limit for mesh refinement from which further refinement can no longer yield a more accurate result. The result obtained by this grid is referred to as grid-independent result.

1.3.2 Large Eddy Simulation

In a turbulent fluid flow, it is observed that there are many different length scales. These length scales are representative of eddies' scales in the motion. It is believed that the large scales, receive the energy from the main flow that is delivered via smaller scales to the smallest scales where it is dissipated. This phenomenon is called cascade process.

The idea of LES comes from this fact that the small scales, regardless of the type of flow and boundary conditions, show an isotropic behavior. So if the large scales are resolved, it is accurate enough to model the small scales which are called the sub-grid scales or SGS. In order to get reasonably good accuracy it is shown that the grid should be fine to such extent that the cut-off takes place in the inertial subrange (see Figure 1.3). Cut-off is the wave number which is representative of

the smallest resolved eddy length. Consequently, twice of the smallest mesh size is the size of the smallest eddy length scale that the grid can resolve.

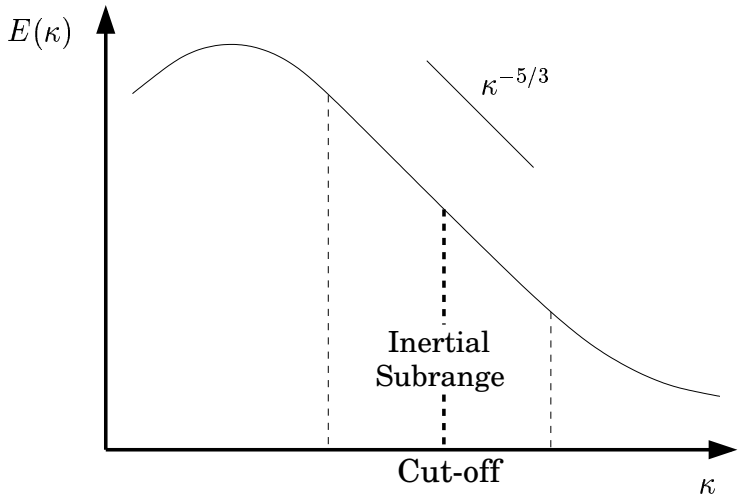

Figure 1.3: Energy spectra.

Important difference between RANS and LES governing equations is the method of filtering. While in RANS the filtering is performed in time, in LES, the equations are filtered in space. The filtering process is an implicit definition, meaning that the value of any parameter in each cell of the grid is a spatial average of that parameter inside the cell. Another difference compared to RANS is that as turbulence is a time dependent three dimensional phenomenon, the governing equations in LES should also be solved in unsteady, three dimensional format. These differences make the LES much more expensive than RANS models. Another fact regarding LES is that the grid is supposed to be fine enough to cover some part of scales in the inertial subrange. According to Kaltenbach *et al.* (1999), an LES simulation based on spectral methods over moderate Reynolds number range, will produce reliable results if the near wall spacing base on wall units are of the order of $\Delta x^+ = 100$ for stream-wise direction and $\Delta z^+ = 30$ in the span-wise direction. The minimum spacing must be reduced by at least a factor of two in order to achieve results of comparable quality using second-order finite difference method (Kaltenbach *et al.*, 1999). Also, the extent of grid in the span-wise direction should be such that the two point correlation of all important parameters in this direction reach to the zero.

1.3.3 Direct Numerical Simulation

Technically, there is no difference between LES and DNS but the cut-off location. When all the scales from largest to smallest are resolved, a direct numerical simulation is achieved. In this sense, the only difference between an LES and a DNS problem is the grid which is employed. This method requires a grid resolution as fine as the Kolmogorov micro-scale. DNS is more time consuming compared to LES so except for very special simple flows it is too expensive to be implemented.

1.4 Previous Investigations

Natural convection heat transfer has been studied experimentally as well as numerically and analytically during past decades. Many experiments on the laminar natural heat transfer boundary layer have been performed and the results are shown by Burmeister (1993). These experiments have been conducted for various ranges of Prandtl numbers and many useful correlations between Nusselt and Rayleigh numbers are proposed.

Similarity solution for laminar natural heat transfer boundary layer at different Prandtl numbers which was carried out by Ostrach (1952), yielded results that were in good agreement with previous experiments.

Turbulent natural convection boundary layer next to a heated vertical surface was analyzed by George & Capp (1979) by classical scaling arguments. In this theoretical investigation, the boundary layer is treated in two parts. An inner region in which the mean convection terms are negligible and is identified as constant heat flux layer and an outer region which constructs most of the boundary layer in which conduction terms are considered negligible. In this work, universal velocity and temperature profiles for asymptotic values of Rayleigh number when approaches infinity are suggested for both constant heat flux and constant temperature boundary conditions. The proposed theory was modified later by Wosnik & George (1995) and it was claimed that the new scaling functions were valid both in the limit of infinite Rayleigh number and for any position downstream well into the turbulent regime. It was also shown that the boundary layer showed no linear expansion for moderate Rayleigh numbers but asymptotically lost its stream-wise inhomogeneity where it expanded linearly.

Experiments of the turbulent natural heat transfer boundary layer in air were conducted by Warner & Arpaci (1968) and Cheesewright (1968). Some experiments were also carried out in different liquids by Lock & Trotter (1968), Vliet & Liu (1969), Fujii *et al.* (1970) and Kutateladze *et al.* (1972). In all of these experiments, the overall characteristics of the natural convection were studied.

Turbulent transport in a natural convection along a vertical flat plate was experimentally studied by Kitamura *et al.* (1985) and it was shown that the large eddy motions play an important role on the turbulent transport. Later, Tsuji & Nagano (1988*a*) performed an experimental study of natural convecting heat transfer boundary layer in more detail compared to previous researches. Characteristics of the near wall region was studied and applicability of the conventional analogy between heat and momentum transfer and the concept of the viscous sublayer for natural convection were investigated. The structure of turbulent natural convection boundary layer was studied further by Tsuji & Nagano (1988*b*) and it was shown that this phenomenon has a unique turbulent structure which is rarely seen in other turbulent boundary layers. The results suggest that for values of y^+ between 20 to 100, $\overline{u'v'}$ is not correlated with the mean velocity gradient, i.e. $\partial U/\partial y$.

Turbulent natural convection around a heated vertical slender cylinder was studied by Persson & Karlsson (1996) and new turbulent structures were presented for the near wall region. It was shown that there exist a region of negative shear stress close to the cylinder contrary to the measurements of Tsuji & Nagano (1988*b*).

Low turbulence natural convection in an air filled square cavity was studied and the results for the thermal and fluid flow fields and turbulence quantities were published by Tian & Karayiannis (2000*a*) and Tian & Karayiannis (2000*b*), respectively. The experiments were conducted at a relatively low Rayleigh number $Ra = 1.58 \cdot 10^9$ and the contour plot of the thermal field and a vector plot of air flow in the cavity are reported for the first time. It is believed that in this experiment, the level of turbulence has been quite low, and the flow has been only transitional with a stratified quiescent flow in the core.

Another experiment in cavity was set up by Betts & Bokhari (2000). It consisted of an enclosed tall cavity where in the core region, flow was fully turbulent. The experiment was performed at two different Rayleigh numbers, $Re = 0.86 \cdot 10^6$ and $Re = 1.43 \cdot 10^6$, based on the cavity width. The advantage of having a tall and thin cavity was that it made it easier to achieve two dimensional results.

Natural convecting boundary layer has also been studied numerically. Many investigations have been carried out and useful results are proposed. The difficulties and controversial modeling issues within the framework of the second-moment closures are discussed by Hanjalic (1994) and some suggestions for the future researches by considering many test flows, have been made.

Considering RANS computations, a $v^2 - f$ and a $k - \epsilon$ model were compared with the experimental data for two different geometries by Tieszen *et al.* (1998). The two considered geometries were a vertical flat plate and a differentially heated cavity. Three different treatments of buoyancy/turbulence coupling were compared and it was shown that $v^2 - f$ model together with employment of a buoyant production term which was defined based on generalized gradient diffusion hypothesis yielded the best result.

Computation of turbulent buoyant flow in a cavity was carried out by Peng & Davidson (1999) and a low Reynolds number $k - \omega$ model was employed in the computations. It is mentioned that the customary $k - \epsilon$ models are not capable of giving grid independent prediction owing to the transition regime especially for moderate Rayleigh numbers between 10^{10} to 10^{12}. It is shown that this grid independency comes from buoyancy source term for the turbulence kinetic energy that exhibits strong grid sensitivity. This problem was fixed by introducing a damping function in buoyant production term.

LES of natural convection in concentric horizontal annuli was studied by Miki *et al.* (1993) and the results were compared by available experimental results. The maximum Rayleigh number based on the gap width was $1.18 \cdot 10^9$. It was shown that by ignoring SGS model in the governing equations, very different results for fluctuating quantities were achieved, although the results for overall flow quantities such as velocity and temperature remained reasonable. It was shown that the accumulation of energy in small scales caused this problem. Also it was shown that by increasing the Smagorinsky constant from 0.1 to 0.2, the ratio of SGS energy to grid scale energy increased drastically.

Peng & Davidson (1998) studied the effect of different SGS models and proposed a new SGS model for buoyancy affected turbulent flows. The three studied SGS models were a scalar model which has no term to take the effect of buoyancy into account, a buoyancy model which was proposed by Eidson (1985) and a modified model based on the buoyancy model. The motivation for proposing the modified model was the resulting non-real solutions to the cases that buoyancy term was larger

than strain rate tensor. It was shown that all models despite of very different coefficients gave similar results when applied to a Rayleigh-Bénard problem with a Rayleigh number equal to $3.8 \cdot 10^5$. Low influence of small scales on the large scales and low turbulence level of the considered Rayleigh-Bénard problem was mentioned to be the likely reasons for the similarity of results.

Ningyu *et al.* (2000) proposed a new dynamic SGS model for LES of stratified flows. The new model was then applied to a Rayleigh-Bénard problem at different Richardson numbers and it was shown that for Richardson numbers larger than a critical 0.06 value, the flow showed a laminar behavior. The obtained critical Richardson number was shown to be in good agreement with theoretical value of 0.0554.

Zhang & Chen (2000) proposed a new dynamic SGS model which is based on a new defined averaging method in order to calculate the dynamic SGS viscosity coefficient when there exist no homogeneous direction in the considered computational geometry. Motivation for proposed model was that due to high fluctuations of the SGS coefficient in dynamic models, convergence is highly unstable. The proposed model is claimed to be useful for indoor airflows in which there is generally no homogeneous direction involved. The performance of the model is investigated by comparing the obtained results for three different cases of pure natural, forced and mixed convection in different three dimensional cavities and existing experimental results.

LES of a turbulent rotating convective flow was performed by Cui & Street (2001). In this study, the adopted geometry consisted of a circular tank of radius $R_o = 0.48m$ and the fluid was water. A heat exchanger of radius $R_i = 0.2m$ was set up below the tank. Results were obtained for different rotational speeds and buoyancy heat fluxes. It was shown that neither the angular velocity nor buoyancy flux affect the growth of the conductive layer which forms over the heating plate below the tank. It is also shown that the convective rings which form near bottom of the tank, look more uniform with increasing angular velocity and the time that it takes for the rings to reach the top of the tank is independent of the angular velocity. Furthermore it was shown that the number of convective rings depends on the buoyancy flux.

Peng & Davidson (2001*b*) studied the LES of turbulent flow in a confined cavity and compared the results with the experiment of Tian & Karayiannis (2000*a*) and Tian & Karayiannis (2000*b*). It was shown that mean flow quantities were in good agreement with the experimental results, however, there were some discrepancies in the prediction of

turbulence statistics especially in the shear layer region between the wall boundary layer flow and the cavity core region. It is suggested that special attention should be paid to the flow physics and numerical treatment in this region. A comparative study of LES of turbulent buoyant flow in a cavity with different SGS models and grid resolutions was also performed by Peng & Davidson (2001a). It was shown that although the proposed SGS model was able to predict mean flow quantities, it was unable to recreate the turbulence quantities particularly in the core region. It was also shown that the energetic flow structures which are enhanced by buoyancy in the boundary layer along the heated and cooled walls of the cavity, exist in the outer layer neighboring the nearly stagnant core region of the cavity. Existence of a k^{-3} buoyancy subrange next to the $k^{-5/3}$ inertial subrange was confirmed by the results. It was suggested that a span-wise mesh spacing of $\Delta z^+ \approx 20$ is appropriate to resolve the energetic, coherent structures in the boundary layer. Peng & Davidson (2002) in continuation of previous works, proposed a new non-linear SGS heat-flux model. The model is to some extent similar to a scale-similarity model subjected to a Taylor expansion for the filtering operation. The model was examined in an infinite vertical channel with differentially heated walls and it was shown that very encouraging results compared to DNS and experimental results were achieved.

Natural convection boundary layers are also studied by DNS. As it is very hard to resolve the smallest scales, only simple geometries have been studied so far. Iida & Kasagi (1997) studied the Rayleigh-Bénard problem with cross stream flow and observed remarkable phenomena in this particular type of flow. They showed that the large-scale thermal convection involving the thermal plumes diminishes the quasi-coherent stream-wise vortices, which consequently results in an increment in the bulk mean velocity and decreases turbulent friction coefficient. The effect of the Prandtl number on the kinetic energy of turbulence was also studied and it was shown that the kinetic energy of turbulence is a non-linear function of Prandtl number.

Using DNS, Natural convection between two vertical differentially heated walls was studied by Nieuwstadt & Versteegh (1997). The major topic of investigation in this study was the self similarity behavior of the results following the scaling hypothesis proposed by George & Capp (1979). It was shown that the proposed scaling approach leads to self-similarity for the mean temperature profile but it fails for the mean velocity profile. The adopted geometry dimension in this study was $7.6\pi\delta \cdot 4\pi\delta \cdot 2\delta$ in stream-wise, span-wise and cross stream-wise direc-

tions, respectively. In another study, Versteegh & Nieuwstadt (1998) investigated the turbulent budgets of natural convection in an infinite, differentially heated, vertical channel. It was found that close to the wall, the shear production of turbulence was negative. It was also mentioned that modeling of pressure strain and transport terms in a separated way is not a good idea while the combination of these two terms behaves in a more continuous way especially near wall.

Limiting behavior of turbulent transport of a scalar close to a wall using DNS, was studied by Na & Hanratty (2000). A horizontal channel flow with the lower wall kept at a higher temperature than the upper wall was adopted as the investigating flow and geometry. It was shown that the analogy between momentum and scalar transport can not be used to define the limiting behavior of turbulent diffusivity when $y \to 0$.

DNS of a plane vertical channel flow, in order to study the difference between the case with buoyancy and the case without buoyancy was performed by Davidson *et al.* (2003). It was found that in the case without buoyancy or forced convection case, the turbulent shear stress balances the pressure gradient in the region away from the viscous dominated region. However, in the case with buoyancy or mixed convection case, it is shown that the buoyancy term modifies the shear stress in a way that it is decreased near the hot wall where the flow is ascending and increased near the cold wall where the flow is descending. This is shown to be the case for all normal stresses as well. However, it is shown that $\overline{t'^2}$ behaves in a different way compared to Reynolds stresses. It increases near the hot wall and decreases near the cold wall. Finally, as it was found that turbulent shear stress and normal turbulent heat flux were not correlated to velocity and temperature gradient across the channel, respectively, Reynolds stress models were recommended to be used for buoyancy-affected flows because in these methods, no direct stress-strain coupling is assumed.

1.5 Designing an LES Problem

From previous investigations it can be found that natural convection phenomenon has still a lot of aspects which are not clear and there are some other aspects for which there is no general agreement. Another fact is that there is either no or very few researches on the natural convective boundary layer along a vertical cylinder and most of the studies are performed on the plates or channels or horizontal cylin-

ders. Regarding this and existence of an experimental apparatus in the laboratory of Department, created the motivation for designing an LES problem in order to study the natural convection heat transfer along a vertical cylinder. The schematic diagram of the experimental apparatus is shown in Figure 1.4.

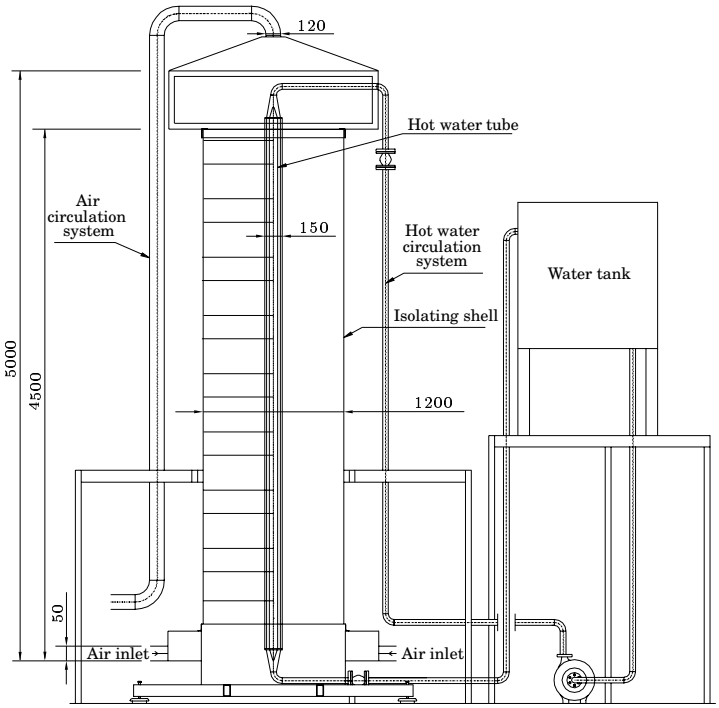

Figure 1.4: Experimental apparatus.

Water temperature is kept at 80^oC and is circulated in counter flow direction respect to the air flow around it. The incoming air, is kept at 25^oC by help of an HVAC unit which is not shown in the figure. This unit feeds air to the inlet, which is located near the bottom of the isolating shell. The reason for feeding air is to prevent stratification. This problem is explained in detail in the next chapter. Both at the inlet and near the outlet at the height of $4.5m$ perforated plates are used in order to make the flow at inlet and outlet smooth and uniform. The maximum local Grashof number reaches approximately $Gr_z = 5 \cdot 10^{11}$ in this apparatus. The reason for choosing such a geometrical configuration is that although an idealized vertical natural convection boundary layer takes place in infinite surroundings, it is impossible to achieve such an ideal condition either in experiments or in numerical calculations. In fact, both experiments and calculations are very sensitive to the location of the infinite boundaries and any disturbances there (Persson &

Karlsson, 1996). Another advantage of this geometrical configuration is that it makes it possible to create a truly two dimensional fluid flow and heat transfer.

1.6 Overview of the Present Study

This work is divided into three major parts. In Chapter 2, a RANS model is applied to a simplified two dimensional geometry which is adopted concerning the experimental apparatus. As the apparatus is not activated yet, its proper operating condition is numerically studied. Simplification of the geometry to such an extent that the change in results is negligible is also an object of this study.

In Chapter 3, the recommended two dimensional geometry of Chapter 2 is converted to a three dimensional geometry and LES of the flow is performed and the results are studied. In order to accelerate the state of the flow to a numerically fully developed condition, the results from the RANS simulations are used as initial condition.

In Chapter 4, DNS of natural convection between two infinite vertical walls is studied. The objective is to qualitatively compare this flow to the flow studied in Chapter 3.

Chapter 2

RANS Modeling

As an engineering point of view, RANS simulations are very time and cost efficient for designing an experimental apparatus or finding optimal operating condition of the apparatus. Besides, when the LES of the flow or heat transfer is a matter of interest, as it is very sensitive to boundary conditions and mesh refinement, it is always worthwhile to get an insight by solving the problem with RANS models. Also it can be very time consuming to reach to a fully developed state while doing LES. So, using the acquired flow and heat transfer results of the RANS simulations, accelerates this process.

Thus, before performing LES, which is very CPU work and time consuming, the different operating conditions of the experimental apparatus, using two dimensional Reynolds Averaged Navier Stokes (RANS) equations, are numerically investigated.

To simulate the desired turbulent flow, two different turbulence models are considered. These two models are based on low Reynolds $k-\omega$ and $k-\varepsilon$ models. As the applicability of these models should first be examined on similar and simple natural convection problems, they are first applied to a confined cavity for which both experimental and LES data are available.

2.1 Governing Equations

The governing equations for the flow inside the shell and tube are the time averaged two dimensional continuity and Navier-Stokes equa-

tions in the cylindrical coordinate system. The Reynolds stress terms are modeled by the help of turbulent kinetic energy and turbulent dissipation equations.

Continuity:

$$\frac{1}{r}\frac{\partial}{\partial r}(r v_r) + \frac{\partial}{\partial z}(v_z) = 0 \tag{2.1}$$

Convective derivative:

$$\mathbf{V}\cdot\nabla = v_r\frac{\partial}{\partial r} + v_z\frac{\partial}{\partial z} \tag{2.2}$$

Laplacian operator:

$$\nabla^2 = \frac{1}{r}\frac{\partial}{\partial r}\left(r\frac{\partial}{\partial r}\right) + \frac{\partial^2}{\partial z^2} \tag{2.3}$$

The r-momentum equation:

$$\begin{aligned}(\mathbf{V}\cdot\nabla)\,v_r = &-\frac{1}{\rho}\frac{\partial p}{\partial r} + \frac{1}{r}\frac{\partial}{\partial r}\left(r\nu_{eff,v}\frac{\partial v_r}{\partial r}\right) - \nu_{eff,v}\frac{v_r}{r^2}\\ &+ \frac{\partial}{\partial z}\left(\nu_{eff,v}\frac{\partial v_r}{\partial z}\right)\end{aligned} \tag{2.4}$$

The z-momentum equation:

$$\begin{aligned}(\mathbf{V}\cdot\nabla)\,v_z = &-\frac{1}{\rho}\frac{\partial p}{\partial z} + g_z\beta(T-T_f) + \frac{1}{r}\frac{\partial}{\partial r}\left(r\nu_{eff,v}\frac{\partial v_z}{\partial r}\right)\\ &+ \frac{\partial}{\partial z}\left(\nu_{eff,v}\frac{\partial v_z}{\partial z}\right)\end{aligned} \tag{2.5}$$

The energy equation:

$$(\mathbf{V}\cdot\nabla)\,T = \frac{1}{r}\frac{\partial}{\partial r}\left(r\nu_{eff,T}\frac{\partial T}{\partial r}\right) + \frac{\partial}{\partial z}\left(\nu_{eff,T}\frac{\partial T}{\partial z}\right) \tag{2.6}$$

Here, the turbulent diffusive cross terms arising from $\frac{\partial}{\partial x_j}\left(\nu_{eff}\frac{\partial v_j}{\partial x_i}\right)$ in which v_j stands for velocity vector, are neglected. The two turbulence models which have been used are the $k-\varepsilon$ model which is proposed by Abe *et al.* (1994) (hereafter referred to AKN model) and $k-\omega$ model of Peng *et al.* (1997) (hereafter referred to PDH model). For the AKN

model the kinetic energy and the dissipation rate of turbulence equations are:

$$(\mathbf{V}\cdot\nabla)\,k = \frac{1}{r}\frac{\partial}{\partial r}\left(r\nu_{eff,k}\frac{\partial k}{\partial r}\right) + \frac{\partial}{\partial z}\left(\nu_{eff,k}\frac{\partial k}{\partial z}\right) + P_k - \varepsilon \tag{2.7}$$

$$(\mathbf{V}\cdot\nabla)\,\varepsilon = \frac{1}{r}\frac{\partial}{\partial r}\left(r\nu_{eff,\varepsilon}\frac{\partial \varepsilon}{\partial r}\right) + \frac{\partial}{\partial z}\left(\nu_{eff,\varepsilon}\frac{\partial \varepsilon}{\partial z}\right) + \frac{\varepsilon}{k}(C_{\varepsilon 1}P_k - C_{\varepsilon 2}f_\varepsilon\varepsilon) \tag{2.8}$$

in which:

$$P_k = 2\nu_t\left[\left(\frac{\partial v_r}{\partial r}\right)^2 + \left(\frac{\partial v_z}{\partial z}\right)^2\right] + \nu_t\left(\frac{\partial v_r}{\partial z} + \frac{\partial v_z}{\partial r}\right)^2 + \nu_t\left(\frac{2}{r^2}v_r^2\right)$$

$$\nu_{eff,v} = \nu + \nu_t$$

$$\nu_{eff,T} = \frac{\nu}{Pr} + \frac{\nu_t}{Pr_t}$$

$$\nu_{eff,k} = \nu + \frac{\nu_t}{\sigma_k}$$

$$\nu_{eff,\varepsilon} = \nu + \frac{\nu_t}{\sigma_\varepsilon}$$

$$\nu_t = C_\mu f_\mu \frac{k^2}{\varepsilon}$$

$$f_\mu = \left\{1 - \exp\left(-\frac{y^*}{14}\right)\right\}^2\left[1 + \frac{5}{R_t^{3/4}}\exp\left\{-\left(\frac{R_t}{200}\right)^2\right\}\right]$$

$$f_\varepsilon = \left\{1 - \exp\left(-\frac{y^*}{3.1}\right)\right\}^2\left[1 - 0.3\exp\left\{-\left(\frac{R_t}{6.5}\right)^2\right\}\right]$$

$$y^* = \frac{u_\varepsilon n}{\nu}, \quad u_\varepsilon = (\nu\varepsilon)^{1/4}, \quad R_t = \frac{k^2}{\nu\varepsilon}$$

$$C_\mu = 0.09, \quad \sigma_k = 1.4, \quad \sigma_\varepsilon = 1.4, \quad C_{\varepsilon 1} = 1.5, \quad C_{\varepsilon 2} = 1.9$$

The value of ε for wall adjacent nodes is set to $\varepsilon_w = 2\nu k/n^2$. For PDH model the kinetic energy and specific dissipation equations are:

$$(\mathbf{V}\cdot\nabla)\,k = \frac{1}{r}\frac{\partial}{\partial r}\left(r\nu_{eff,k}\frac{\partial k}{\partial r}\right) + \frac{\partial}{\partial z}\left(\nu_{eff,k}\frac{\partial k}{\partial z}\right) + P_k - C_k f_k \omega k \tag{2.9}$$

$$\begin{aligned}(\mathbf{V}\cdot\nabla)\,\omega = \frac{1}{r}\frac{\partial}{\partial r}\left(r\nu_{eff,\omega}\frac{\partial \omega}{\partial r}\right) + \frac{\partial}{\partial z}\left(\nu_{eff,\omega}\frac{\partial \omega}{\partial z}\right) + \\ \frac{\omega}{k}(C_{\omega 1}f_\omega P_k - C_{\omega 2}\omega^2) + C_\omega\frac{\nu_t}{k}\left(\frac{\partial \omega}{\partial r}\frac{\partial \omega}{\partial r} + \frac{\partial \omega}{\partial z}\frac{\partial \omega}{\partial z}\right)\end{aligned} \tag{2.10}$$

in which the two last terms in ω-equation are cross diffusion terms and:

$$\nu_{eff,\omega} = \nu + \frac{\nu_t}{\sigma_\omega}$$

$$\nu_t = C_\mu f_\mu k/\omega$$

$$f_\mu = 0.025 + \left\{1 - \exp\left[-\left(\frac{R_t}{10}\right)^{3/4}\right]\right\}\left\{0.975 + \frac{0.001}{R_t}\exp\left[-\left(\frac{R_t}{200}\right)^2\right]\right\}$$

$$f_k = 1 - 0.722\exp\left[-\left(\frac{R_t}{10}\right)^4\right]$$

$$f_\omega = 1 + 4.3\exp\left[-\left(\frac{R_t}{1.5}\right)^{1/2}\right]$$

$$R_t = \frac{k}{\nu\omega}$$

$$C_\mu = 1.0, \quad C_k = 0.09, \quad C_{\omega 1} = 0.42, \quad C_{\omega 2} = 0.075, \quad C_\omega = 0.75$$

$$\sigma_k = 0.8, \quad \sigma_\omega = 1.35$$

Similar to previous model, wall adjacent nodes are set to a value equal to $\omega_w = 6\nu/(C_{\omega 2} n^2)$.

2.2 Numerical Method

The governing equations are solved in steady state conditions and a third order QUICK scheme for momentum equations and second order Van Leer scheme for turbulence models are used to discretize the governing equations (Davidson & Farhanieh, 1995). In order to solve the discretized equations, the SIMPLEC algorithm together with Rhie and Chow interpolation are employed.

2.3 Turbulence Model Assessment

In order to assess the ability of both turbulence models in predicting the fluid flow and heat transfer of typical natural convection problems, the natural convection in a confined square cavity is considered, where both experimental (Tian & Karayiannis, 2000*a*) and LES results (Peng

& Davidson, 2001*b*) exist. The cavity's left and right walls are hot and cold respectively with a temperature difference of 40^oC. The Rayleigh number based on cavity width is about $Ra = 1.58 \cdot 10^9$. The top and bottom walls of the cavity are highly conductive walls which give a temperature distribution along these walls. As the temperature distribution along these two conductive walls were not linear, the temperature boundary condition are taken directly from the experimental values and a 96×96 mesh has been used. Figures 2.1(a), 2.1(b) and 2.2 compare the streamlines of flow inside the cavity by different models.

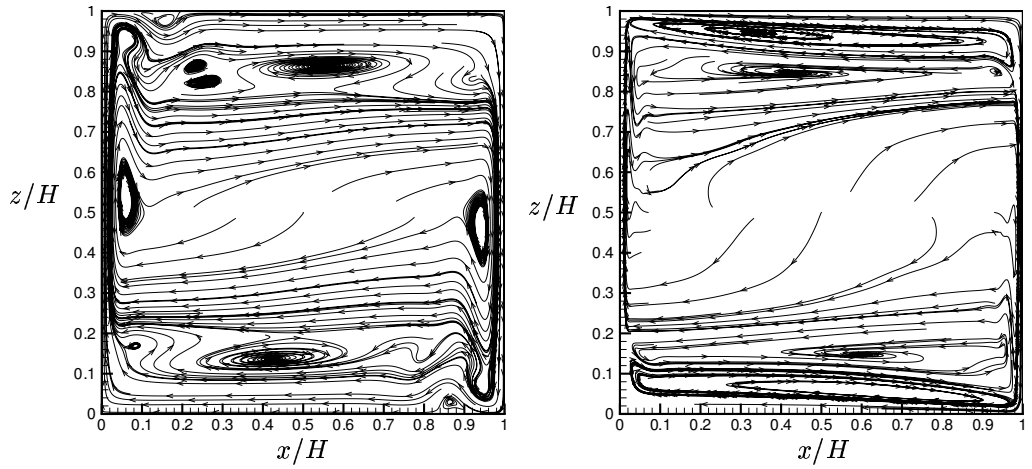

(a) $k - \omega$ (PDH) model. (b) $k - \varepsilon$ (AKN) model.

Figure 2.1: RANS simulation.

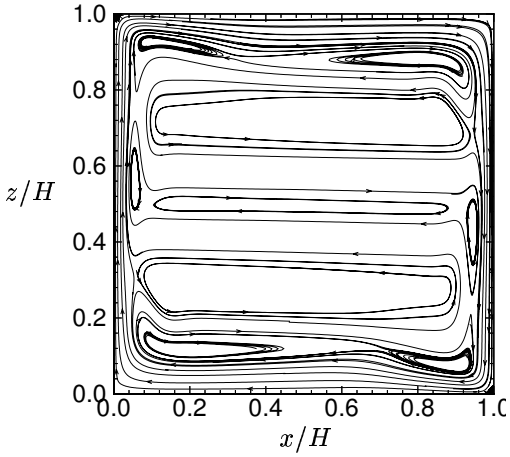

Figure 2.2: LES from Peng & Davidson (2001*b*).

As it is obvious from the figures, the flow structure is predicted differently by different models. However, PDH model result looks more alike

LES model. Furthermore, by studying Figure 2.3 it can be seen that the PDH model is generally in better agreement with experimental data. The reason for why the AKN model and the PDH model give different results is that the transition commencement is predicted differently by the two turbulence models.

2.4 Effect of Inlet Velocity

Among all, one of the most important boundary conditions that plays a vital role on the temperature stratification along the heated tube, is the inlet condition. The reason for this problem is depicted in Figure 2.4.

If the rate of fluid flow inside the boundary layer approaching the outlet ($\dot{m}_{bl}$) becomes larger than the inlet flow rate ($\dot{m}_{in} = \dot{m}_{out}$), some part of fluid ($\dot{m}_{bl} - \dot{m}_{in}$) will recirculate in order to compensate this difference. The recirculating fluid brings hot fluid to the upper part of the domain. Thus, temperature stratification along the outer part of the boundary layer is inevitable, causing the boundary layer growth to be suppressed. However, by increasing the inlet flow rate, a smaller flow recirculation and consequently a smaller temperature stratification is likely to occur. Therefore, the aim is to apply an inlet flow rate large enough to reduce temperature stratification and small enough so that the natural convection remains the dominant phenomenon. So, different inlet velocities are applied and the effect of them are studied.

The computational geometry and boundary conditions are depicted in Figure 2.5, in which all the dimensions are in millimeter. All the walls, except the hot tube which is shown thicker than the other walls, are considered as insulated walls and Neumann boundary condition for temperature is applied to them. The inlet flow is uniform and enters horizontally in the negative radial direction.

The effect of perforated plate is modeled in the calculations knowing that the aspect ratio of *free area of the plate* to *area of passage* is equal to 0.56. Considering this property, the plate causes a pressure drop equal to $\Delta p = K_o \rho v_z^2/2$ where $K_o = 3$ according to Miller (1990).

The calculations are carried out for three different inlet velocities equal to $0.4, 0.5$ and $0.6 m/s$ using the PDH model. Figures 2.6(a) and 2.6(b) show thermal and velocity boundary layer developments. The thermal boundary layer thickness, r_T, is defined as where $(T_w - T)/(T_w - T_\infty) = 0.99$ and for velocity is defined as the location where the fluid velocity

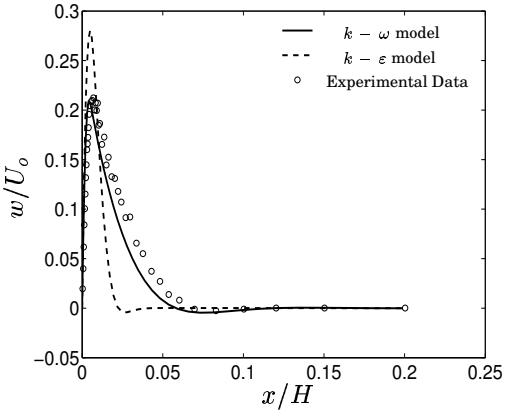

(a) Vertical velocity near hot wall at $z/H = 0.5$.

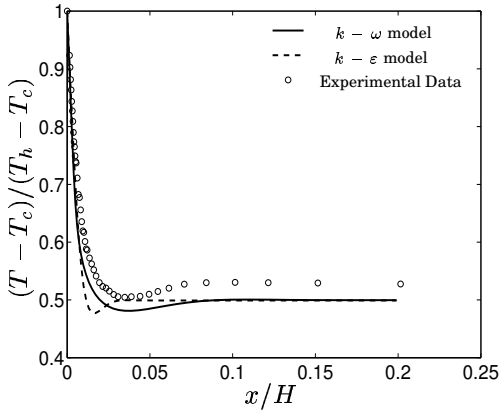

(b) Temperature near hot wall at $z/H = 0.5$.

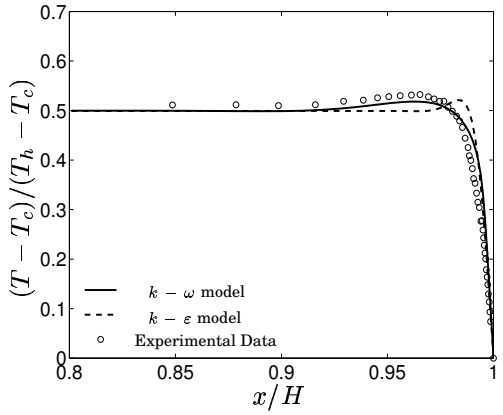

(c) Temperature near cold wall at $z/H = 0.5$.

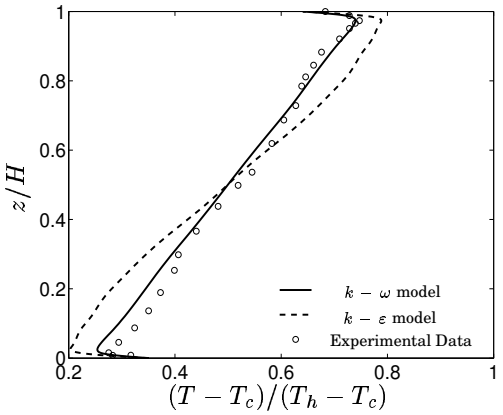

(d) Temperature at $x/H = 0.5$.

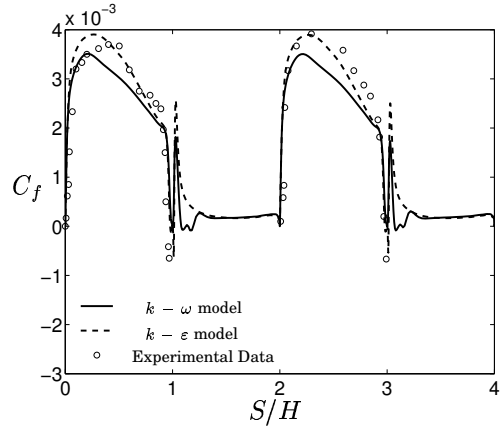

(e) Friction coefficient along cavity walls.

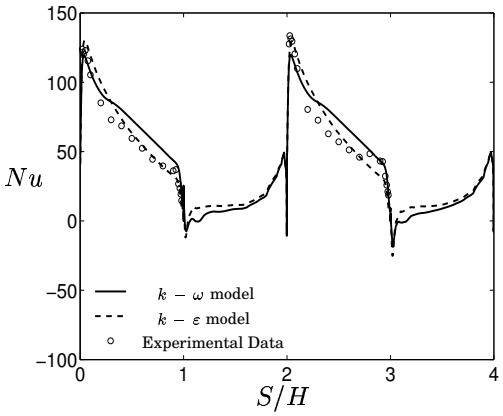

(f) Nusselt number along cavity walls.

Figure 2.3: Results in a square cavity obtained by different models.

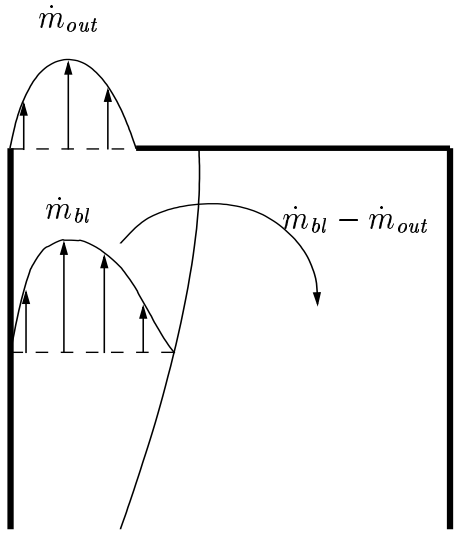

Figure 2.4: Temperature stratification due to recirculation.

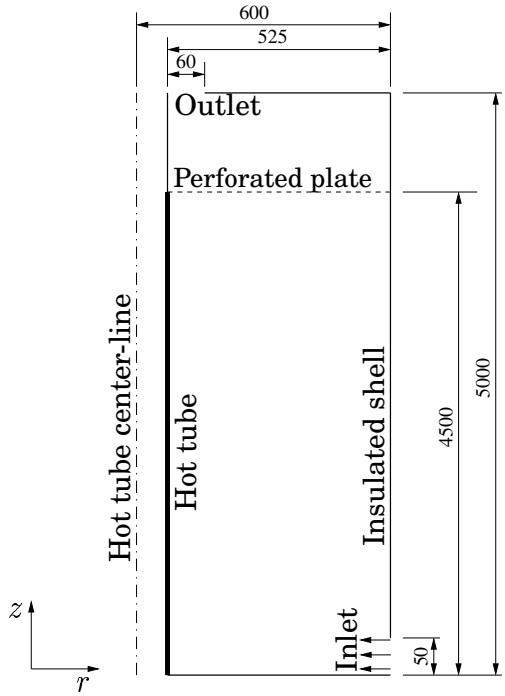

Figure 2.5: Computational geometry.

is half of maximum fluid velocity.

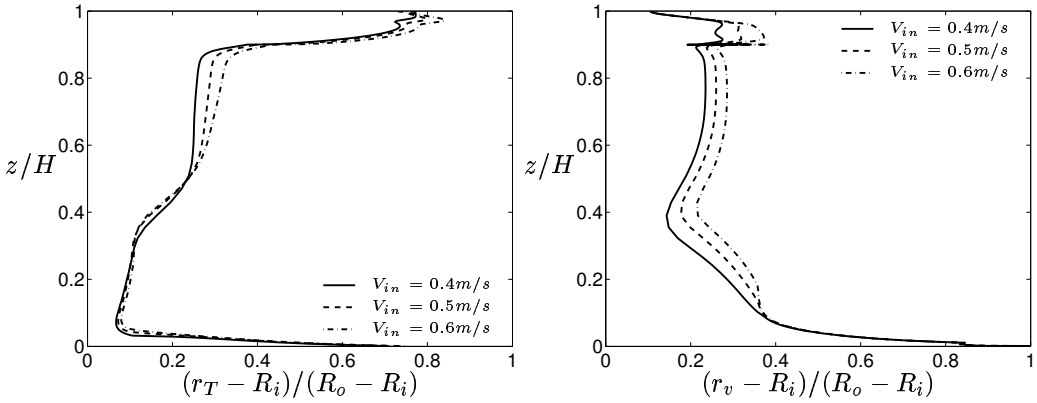

(a) Thermal boundary layer thickness.

(b) Velocity boundary layer thickness.

Figure 2.6: Boundary layer growth for different inlet velocities.

Figure 2.7 compares the local Nusselt number variation, Nu_z, for different inlet velocities, and those obtained experimentally by Tsuji & Nagano (1988*a*) along a flat plate. It can be found that the transition from laminar to turbulent flow, for all cases with different inlet velocities, commences slightly earlier at $Ra_z = 5 \cdot 10^7$ compared to the vertical flat plate. Also another jump in local Nusselt number near $Ra_z = 2 \cdot 10^{10}$ is predicted by the RANS simulations. This jump is related to a recirculation region near the outer shell which extends up to height of $z = 1.4m$ for which $Ra_z = 1 \cdot 10^{10}$ (see Figure 2.7). From this height, as the recirculating region starts to vanish, the actual flow passage widens, causing expansion in the boundary layer. Examination of this region shows that the turbulent viscosity has severely increased which causes the turbulent diffusion to increase. In turn, the wall adjacent fluid temperature decreases causing the local Nusselt number to increase.

In Figure 2.8 the amount of temperature stratification at different radii for different inlet velocities are shown. From the figures, a larger temperature stratification for smaller inlet velocity is perceivable.

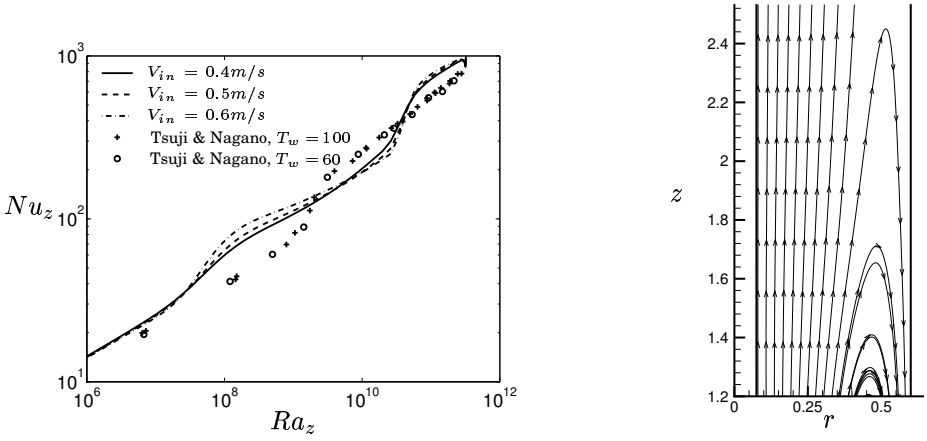

Figure 2.7: Heat transfer rate for different inlet velocities (left) and recirculating region which causes a sudden increase in local Nusselt number (right).

2.5 Effect of Perforated Plate

For sake of simplicity it was of particular interest to investigate the effect of perforated plate and the possibility of its elimination in the future LES simulations. Thus, a new geometry without perforated plate and a reduced $4.5m$ height with the same outlet was introduced. Figures 2.9(a) and 2.9(b) compare the thermal and velocity boundary layers growth of the two geometries with the inlet velocity (V_{in}) equal to $0.6m/s$.

Except for a very small region at the highest part of geometry, no difference between the results of the two different geometries is recognizable. This feature is still valid for the Nusselt number as it is shown in Figure 2.10.

The grids which were used for the different geometries were 120×220 and 120×136 in r and z directions for the geometries with and without perforated plate respectively. The latter obviously, saves a great deal of computational time. Another disadvantage of having the perforated plate included in the computations is that it can create numerical problems in the future LES simulations. Also it was observed that by decreasing the grid size to 96×96 the changes in the results were less than five percent.

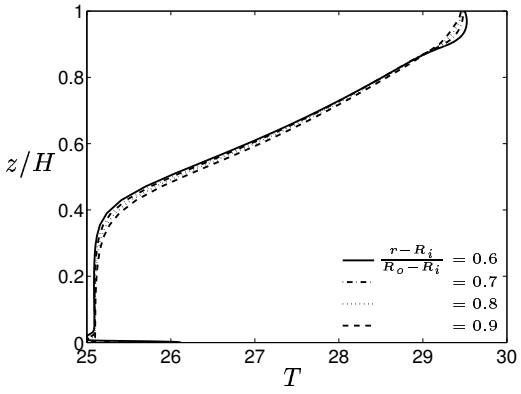

(a) $V_{in} = 0.4m/s$.

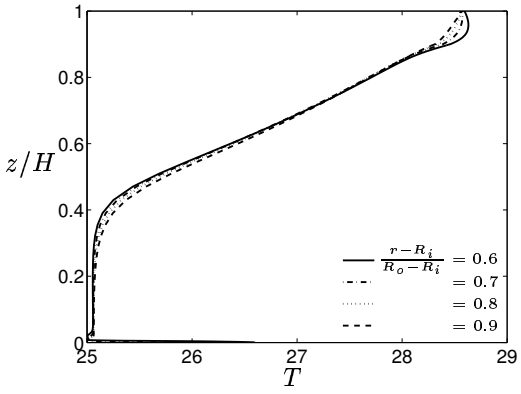

(b) $V_{in} = 0.5m/s$.

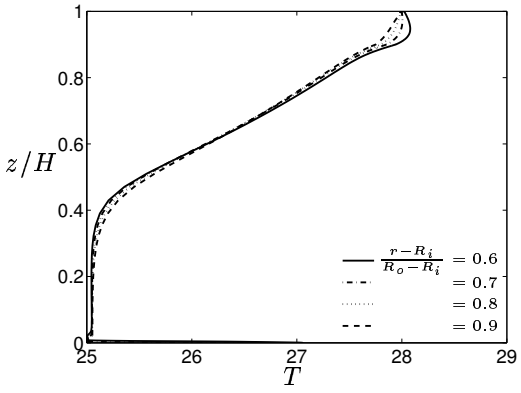

(c) $V_{in} = 0.6m/s$.

Figure 2.8: Temperature stratification.

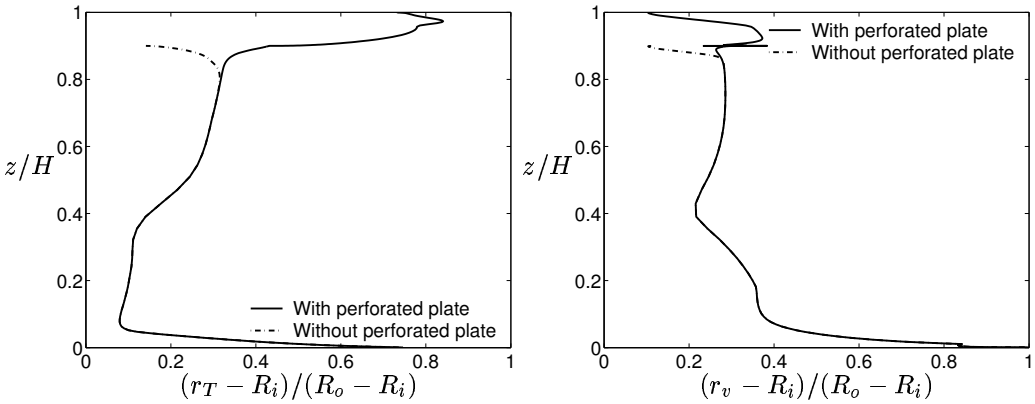

(a) thermal boundary layer.

(b) velocity boundary layer.

Figure 2.9: Boundary layer growth for different geometries.

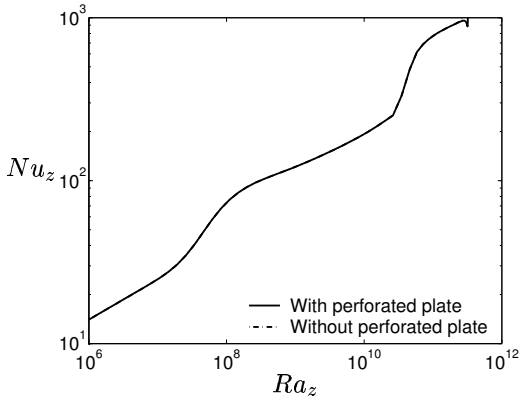

Figure 2.10: Heat transfer rate for different geometries.

2.6 Effect of Outlet Dimension

In this section, the increasing effect of the outlet dimension is studied. When the outlet dimension is $60mm$, the flow accelerates toward the outlet causing a rapid increase in Nusselt number as well as friction coefficient. As a result, relatively large radial velocities, v_r, will be generated near the outlet region. Although this is not a problem in the present 2D RANS calculations, it can introduce a problem in LES simulations, since the largest CFL number occurs in this region. This makes the LES simulations unnecessarily expensive because of the limitation of choosing small computational time steps. To overcome this problem a remedy is to increase the outlet dimension such that this increase does not affect the characteristics of fluid flow in the inner part of computational domain.

Comparing different outlet boundary conditions, the results are shown in Figures 2.11(a) and 2.11(b) which are in complete agreement with each other. Needless to say, the same agreement is valid for heat transfer coefficient in Figure 2.12.

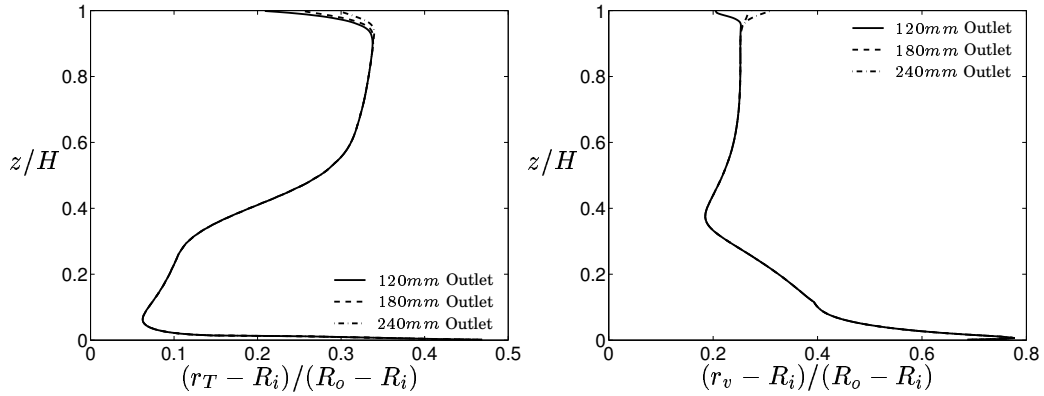

(a) thermal boundary layer.

(b) velocity boundary layer.

Figure 2.11: Boundary layer growth for different outlet dimensions.

This enables us to study the flow field and heat transfer, considering hypothetical outlet dimension without expecting significant discrepancies in achieved results compared to the original geometry configuration.

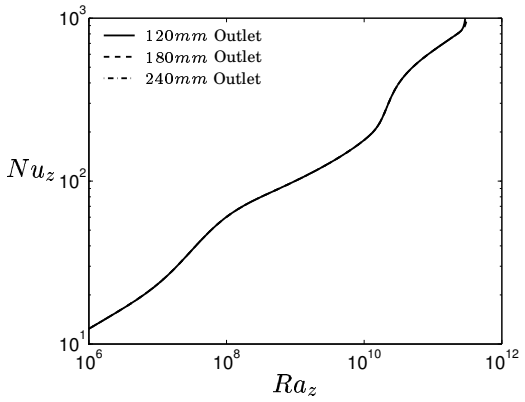

Figure 2.12: Heat transfer rate for different outlet dimensions.

2.7 Effect of Inlet Dimension

One of the major advantages of numerical methods is that we can easily change or modify different part of the geometry in order to design, compare or anticipate the fluid flow and heat transfer behavior. In this study it was of particular interest to study a geometry with a doubled inlet dimension while the inlet flow rate was kept constant so that a lower initial momentum was supplied at the inlet. Figures 2.13(a) and 2.13(b) compare the thermal and velocity boundary layers growth and Figure 2.14 compares the heat transfer rate from the heated inner tube of the two geometries. The inlet condition for the imaginary apparatus is adjusted such that the flow is comparable to the original apparatus with $0.5m/s$ inlet air velocity.

When the inlet dimension is doubled, the inlet velocity is reduced by a factor of two and as a result the transition from laminar to turbulent is smoother. Again near the outlet, the Nusselt number increases due to fluid acceleration similar to the original configuration but in a smoother way. Furthermore, the commencement of transition region has slightly retarded.

2.8 Effect of Outer Shell Radius

In this section the doubling effect of the apparatus cross sectional area in the way that inlet flow rate remains approximately constant, is investigated and the results are depicted in Figures 2.15 and 2.16, in which R_{out} stands for the outer shell radius. The inlet condition for the

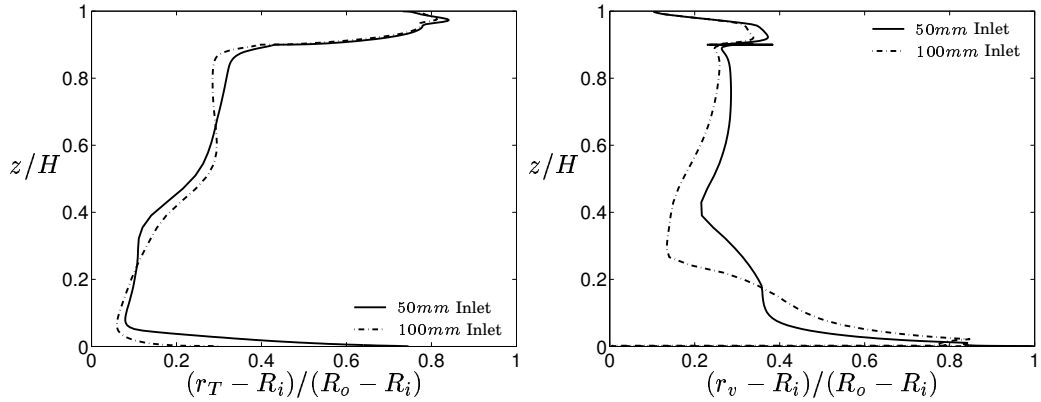

(a) thermal boundary layer.

(b) velocity boundary layer.

Figure 2.13: Boundary layer growth for different inlet dimensions, with perforated plate.

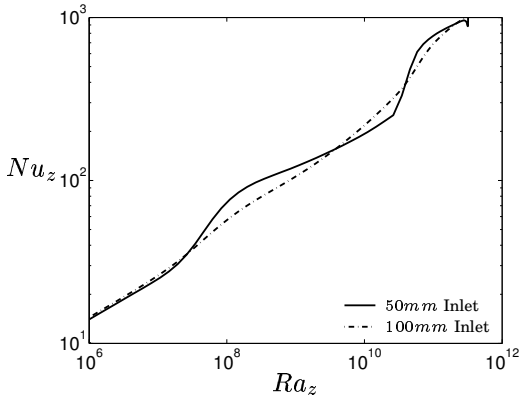

Figure 2.14: Heat transfer rate for different inlet dimensions, with perforated plate.

imaginary apparatus is adjusted such that it is comparable to the real apparatus with $0.6m/s$ inlet air velocity but the mesh size and stretching factors are the same for both cases.

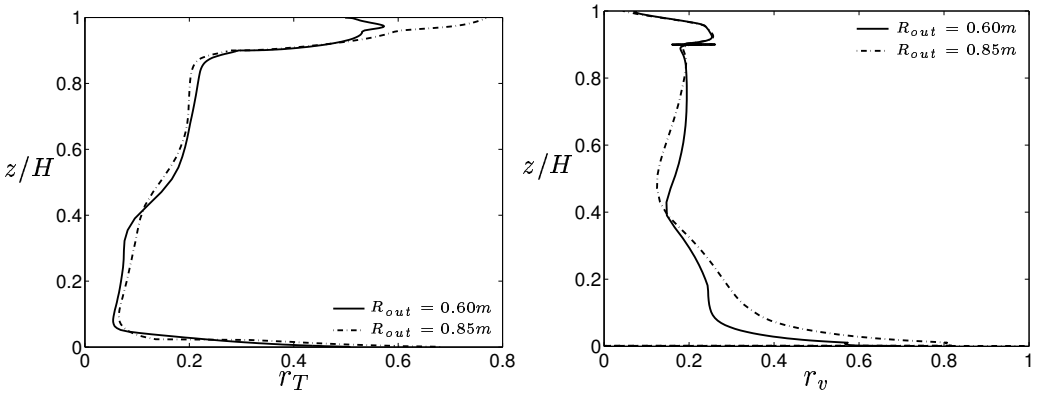

(a) thermal boundary layer.

(b) velocity boundary layer.

Figure 2.15: Boundary layer growth for different shell radii, with perforated plate.

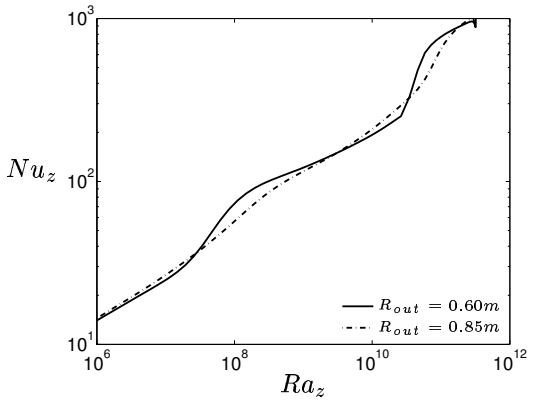

Figure 2.16: Heat transfer rate for different shell radii, with perforated plate.

In this case, as the geometries have different widths, the radial coordinate is not normalized. Once again, like the last case, by doubling the cross sectional area, the typical velocities approximately decrease by a factor of two at the middle part of the rig. This makes the forced convection heat transfer to become less effective and consequently a smoother retarded transition occurs.

2.9 Conclusions

The objective of the present work was to study the effect of inlet boundary conditions and geometrical parameters for a shell and tube configuration. The present work is a pre-study for a comprehensive investigation of this flow using both LES and experiment. Different inlet velocities were applied and different boundary layer growth along the heated tube were observed and it was shown that the larger the inlet velocity becomes, the larger the Nusselt number becomes. Especially near the transition region this difference is large and gradually vanishes in the fully turbulent region.

As the inclusion of the perforated plate in LES may cause some numerical problems, the eliminating effect of the plate was studied. The obtained results showed that except for the very end part of the geometry no significant difference could be observed.

Having a very small outlet causes flow acceleration near the outlet. This means that in LES, a large CFL number is unavoidable. So, the effect of outlet size on the fluid flow and heat transfer was studied and no important difference between different geometries was observed.

Because of the inlet position of the shell and tube, a large vortex at the right half of the geometry close to the shell was formed. To study its effect, one case with doubled inlet size and one with doubled shell and tube effective area cross section were investigated. In both cases the inlet flow rate was kept constant. In the former case it was found that because of smaller inlet velocity, the velocity boundary layer was thinner while no significant change in the thermal boundary layer was found showing that the mixed convection heat transfer was dominated by natural convection in both cases. However near the middle part of the shell and tube, the boundary layers were found to be thicker. This is probably due to less temperature stratification in this case. In the latter case, however, while the thermal boundary layer was not changed significantly, the velocity boundary layer became thicker near transition region. In both cases, the transition to turbulence was smoother compared to the baseline case.

In Figures 2.17(a) and 2.17(b) the variation of v^+ and T^+ at different Gr_z numbers for the case with $0.6m/s$ inlet velocity is compared. While in Figure 2.17(a) it is shown that the assumption of $v^+ = r^+$ is strictly valid for $r^+ \leq 1$, in Figure 2.17(b) the validity of $T^+ = Pr\ r^+$ for values of $r^+ \leq 5$ is shown which is in agreement with Tsuji & Nagano (1988a).

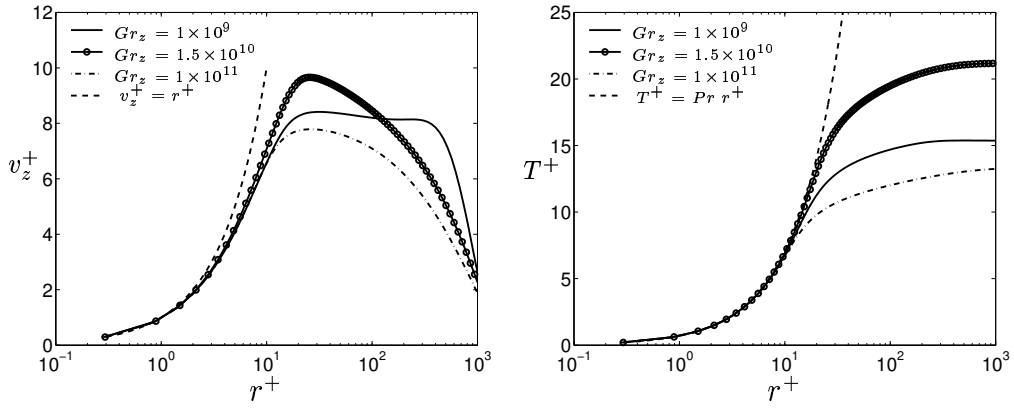

(a) Velocity profile.

(b) Temperature profile.

Figure 2.17: Velocity and temperature profiles.

Finally, in Figure 2.18 the amount of shell and tube energy exchange rate versus inlet velocity of the facility is shown. As it could be expected, the amount of energy consumption rate is increased with inlet velocity increase.

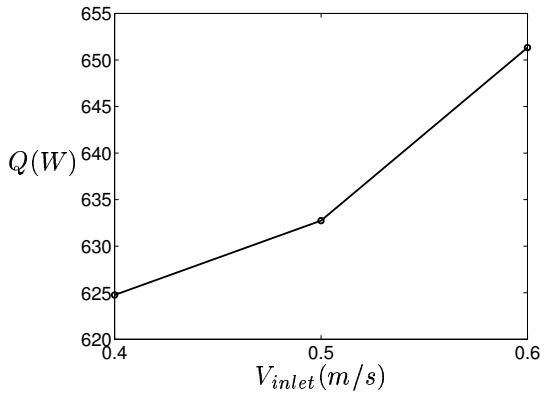

Figure 2.18: Energy exchange rate.

Chapter 3

Large Eddy Simulation

Large Eddy Simulation can be considered as a compromise between accuracy and time compared to the conventional eddy viscosity models and Direct Numerical Simulation method. Alike DNS, the governing equations have an unsteady characteristic in order to capture the large scale turbulence. However, the mesh does not need to be as fine as DNS. In order to advance the flow to become fully developed in time, it is even possible to start the calculations from an initial value obtained from conventional eddy-viscosity models.

To study the natural convection boundary layer along a vertical cylinder, both simplified geometry and initial values for mean flow parameters were adopted from the RANS modeling for which the results were presented in the previous chapter. Several different domains with different span-wise extension in order to obtain a domain independent result are studied. Different grid sizes are studied to make sure that the cut-off takes place at the inertial subrange.

3.1 Governing Equations

The governing equations are the space-averaged three dimensional continuity, Navier-Stokes and energy equations in the cylindrical coordinate system. Smagorinsky model is used to model the subgrid-scale eddies.

Continuity:

$$\frac{1}{r}\frac{\partial}{\partial r}(r\overline{v}_r) + \frac{1}{r}\frac{\partial}{\partial \theta}(\overline{v}_\theta) + \frac{\partial}{\partial z}(\overline{v}_z) = 0 \tag{3.1}$$

Convective time derivative:

$$\mathbf{V}\cdot\nabla=\overline{v}_r\frac{\partial}{\partial r}+\frac{1}{r}\overline{v}_\theta\frac{\partial}{\partial\theta}+\overline{v}_z\frac{\partial}{\partial z} \tag{3.2}$$

Laplacian operator:

$$\nabla^2=\frac{1}{r}\frac{\partial}{\partial r}\left(r\frac{\partial}{\partial r}\right)+\frac{1}{r^2}\frac{\partial^2}{\partial\theta^2}+\frac{\partial^2}{\partial z^2} \tag{3.3}$$

The r-momentum equation:

$$\begin{aligned}&\frac{\partial\overline{v}_r}{\partial t}+\left(\mathbf{V}\cdot\nabla\right)\overline{v}_r-\frac{1}{r}\overline{v}_\theta^2=-\frac{1}{\rho}\frac{\partial p}{\partial r}+\frac{1}{r}\frac{\partial}{\partial r}\left(r\nu_{eff,v}\frac{\partial\overline{v}_r}{\partial r}\right)+\\&\frac{1}{r^2}\frac{\partial}{\partial\theta}\left(\nu_{eff,v}\frac{\partial\overline{v}_r}{\partial\theta}\right)+\frac{\partial}{\partial z}\left(\nu_{eff,v}\frac{\partial\overline{v}_r}{\partial z}\right)-\nu_{eff,v}\frac{\overline{v}_r}{r^2}-\frac{2}{r^2}\nu_{eff,v}\frac{\partial\overline{v}_\theta}{\partial\theta}\end{aligned} \tag{3.4}$$

The θ-momentum equation:

$$\begin{aligned}&\frac{\partial\overline{v}_\theta}{\partial t}+\left(\mathbf{V}\cdot\nabla\right)\overline{v}_\theta+\frac{1}{r}\overline{v}_r\overline{v}_\theta=-\frac{1}{\rho r}\frac{\partial p}{\partial\theta}+\frac{1}{r}\frac{\partial}{\partial r}\left(r\nu_{eff,v}\frac{\partial\overline{v}_\theta}{\partial r}\right)+\\&\frac{1}{r^2}\frac{\partial}{\partial\theta}\left(\nu_{eff,v}\frac{\partial\overline{v}_\theta}{\partial\theta}\right)+\frac{\partial}{\partial z}\left(\nu_{eff,v}\frac{\partial\overline{v}_\theta}{\partial z}\right)-\nu_{eff,v}\frac{\overline{v}_\theta}{r^2}+\frac{2}{r^2}\nu_{eff,v}\frac{\partial\overline{v}_r}{\partial\theta}\end{aligned} \tag{3.5}$$

The z-momentum equation:

$$\begin{aligned}&\frac{\partial\overline{v}_z}{\partial t}+\left(\mathbf{V}\cdot\nabla\right)\overline{v}_z=-\frac{1}{\rho}\frac{\partial p}{\partial z}+g_z\beta(T-T_{ref})+\\&\frac{1}{r}\frac{\partial}{\partial r}\left(r\nu_{eff,v}\frac{\partial\overline{v}_z}{\partial r}\right)+\frac{1}{r^2}\frac{\partial}{\partial\theta}\left(\nu_{eff,v}\frac{\partial\overline{v}_z}{\partial\theta}\right)+\frac{\partial}{\partial z}\left(\nu_{eff,v}\frac{\partial\overline{v}_z}{\partial z}\right)\end{aligned} \tag{3.6}$$

The energy equation:

$$\begin{aligned}&\frac{\partial\overline{T}}{\partial t}+\left(\mathbf{V}\cdot\nabla\right)\overline{T}=\\&\frac{1}{r}\frac{\partial}{\partial r}\left(r\nu_{eff,T}\frac{\partial\overline{T}}{\partial r}\right)+\frac{1}{r^2}\frac{\partial}{\partial\theta}\left(\nu_{eff,T}\frac{\partial\overline{T}}{\partial\theta}\right)+\frac{\partial}{\partial z}\left(\nu_{eff,T}\frac{\partial\overline{T}}{\partial z}\right)\end{aligned} \tag{3.7}$$

in which:

$$\nu_{eff,v}=\nu+\nu_{sgs}$$

$$\nu_{eff,T} = \frac{\nu}{Pr} + \frac{\nu_{sgs}}{Pr_t}$$

$$\nu_{sgs} = (C_S\Delta)^2 f_\mu \sqrt{2\overline{s}_{ij}\overline{s}_{ij}}$$

$$\Delta = (\Delta\mathcal{V})^{1/3} = (\Delta r \times \Delta\theta \times \Delta z)^{1/3}$$

$$2\overline{s}_{ij}\overline{s}_{ij} = 2\left[\left(\frac{\partial\overline{v}_r}{\partial r}\right)^2 + \left(\frac{1}{r}\frac{\partial\overline{v}_\theta}{\partial\theta} + \frac{\overline{v}_r}{r}\right)^2 + \left(\frac{\partial\overline{v}_z}{\partial z}\right)^2\right] +$$
$$\left[\left(\frac{1}{r}\frac{\partial\overline{v}_r}{\partial\theta} + \frac{\partial\overline{v}_\theta}{\partial r} - \frac{\overline{v}_\theta}{r}\right)^2 + \left(\frac{\partial\overline{v}_r}{\partial z} + \frac{\partial\overline{v}_z}{\partial r}\right)^2 + \left(\frac{\partial\overline{v}_\theta}{\partial z} + \frac{1}{r}\frac{\partial\overline{v}_z}{\partial\theta}\right)^2\right]$$

$$f_\mu = 1 - \exp\left(-\frac{n^+}{25}\right)$$

$$C_S = 0.1, \quad Pr_t = 0.4, \quad Pr = 0.7$$

In the above equations, the turbulent diffusive cross terms arising from $\frac{\partial}{\partial x_j}\left(\nu_{eff}\frac{\partial\overline{v}_j}{\partial x_i}\right)$ in which $\overline{v}_j$ stands for filtered velocity vector, are neglected.

3.2 Computational Geometry

Doing RANS computations, it was shown in the previous chapter that the perforated plate elimination has little effect on the boundary layer growth along the vertical cylinder. This makes the geometry simpler and saves computer memory because there is no need to simulate the flow in the upper part of the geometry above the perforated plate. Another fact was the negligible effect of the outlet dimension. As the outlet becomes larger, the flow decelerates more in that area. This is important in LES computation as the CFL number of each cell is supposed not to exceed a value greater than one. Considering these issues, the adopted geometry is shown in figure 3.1.

3.3 Numerical Method

A conventional finite volume method (Versteegh & Malalasekera, 1995) is used to solve the governing equations. As it is very important not to dissipate the turbulence by conventional numerical schemes, it is customary to discretize the governing equations by central difference

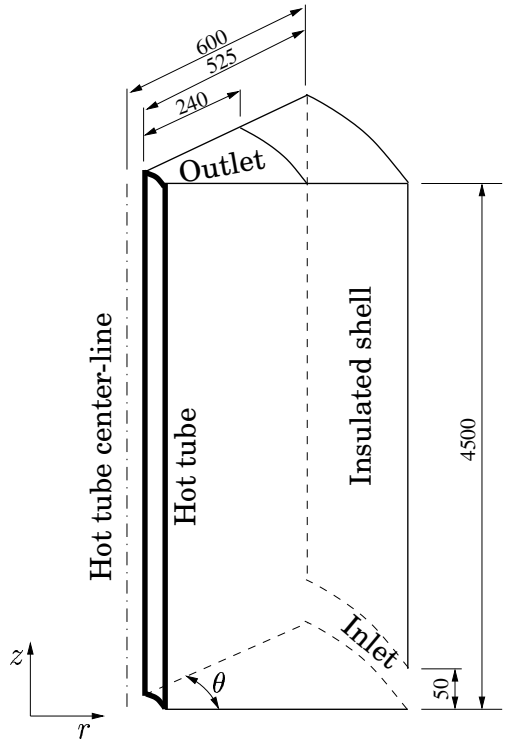

Figure 3.1: Computational geometry.

scheme. However, this approach causes a so called unphysical fluctuation or wiggle problem which is related to the unboundedness of the central difference scheme. Especially, this problem can be encountered in regions where turbulence intensity is not high enough or in laminar regions and in the regions where the grid is not fine enough. Both of these problems occur in the present LES computation near the inlet. If pure central difference scheme is used, these unphysical fluctuations will be generated near the inlet and soon propagate throughout the computational domain. This caused some domain cells to acquire temperatures far below 25^oC. The temperature decrement continued to fall down even to negative temperatures although there were no problem in the code convergence. Also there were no cell in the final averaged result for which the temperature was below 25^oC showing that the conservation of energy had been fulfilled. To remedy this problem, a blend of Van-Leer and central difference scheme with deferred correction (Ferziger & Peric, 1996) can be used (Dahlström & Davidson, 2003), so that the convective flux can be expressed as:

$$\dot{m}u^n_{UDS} + \dot{m}\left[\alpha u^{n-1}_{CDS} - \alpha u^{n-1}_{UDS} + (1-\alpha)u^{n-1}_{UDS_{corr}}\right] \tag{3.8}$$

Here, CDS, UDS and UDS_{corr} stand for the central difference scheme, 1st-order upwind scheme and 2nd-order correction to the lower order upwind scheme respectively. n and $n-1$ stand for current and previous time steps respectively and α is a blending factor which can take a value between zero and one. $\alpha = 0$ gives Van-Leer scheme and $\alpha = 1$ gives central difference scheme with deferred correction. The idea is to set $\alpha = 0$ when a wiggle is detected and $\alpha = 1$ otherwise. As the Van-Leer scheme is bounded, the wiggle will be removed. However, it is difficult to recognize an unphysical wiggle from turbulence. For velocities, the proposed method by Mary & Sagaut (2002) is used to detect the unphysical wiggles. Accordingly, the definition of wiggle is depicted in figure 3.2.

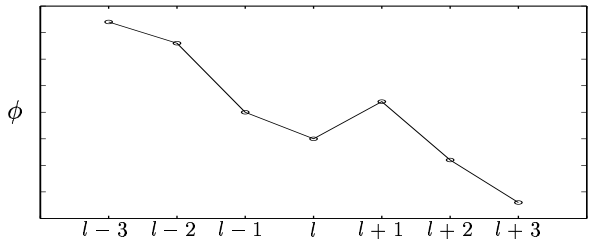

Figure 3.2: Wiggle definition.

The wiggle will be detected at the $l + 1/2$ face when the following correlations are satisfied:

$$\begin{cases} (\phi_{l+1} - \phi_l)(\phi_l - \phi_{l-1}) < 0 \\ \qquad \text{and} \\ (\phi_{l+2} - \phi_{l+1})(\phi_{l+1} - \phi_l) < 0 \end{cases}$$

Here, ϕ stands for a velocity component.

However, for temperature, it is easier to detect a wiggle. As long as there is no source of heat in the flow, the temperature value of each cell can not take a value higher or lower than its neighboring cells. Also, in the absence of source, no computational cell can take a temperature value lower and higher than the coldest and warmest boundaries respectively. In this computations, both criteria are used. For each parameter (v_r, v_z, v_θ, T) at each iteration for each cell, the existence of wiggle in all three directions (stream-wise, span-wise and cross stream-wise) is checked and if there is, the scheme of discretized equations will be modified to Van-Leer scheme via source term. In fact the base scheme for all equations is central difference scheme.

In order to discretize the equations in time, the second-order Crank-Nicolson scheme is used. The numerical procedure is based on an implicit, fractional step technique with a multi-grid pressure Poisson solver (Emvin, 1997) and a non-staggered grid arrangement (Davidson & Peng, 2003).

3.4 Boundary Conditions

As it was explained in the previous section laminar regions may provoke the problem of unphysical fluctuations. In order to have turbulence at the inlet, an instantaneous turbulent velocity field was implemented at the inlet plane. The velocity field was obtained by doing DNS simulation of a channel flow configuration. The data at a cross section plane of the channel for 5000 time steps were extracted and scaled in order to yield the same bulk velocity and height of the inlet. No slip boundary condition is used over all solid boundaries.

For the temperature, Dirichlet boundary condition is applied to the hot tube and at the inlet. The temperature is set to 80^oC and 25^oC on the hot tube and at the inlet respectively. Except for the outlet, homogeneous Neumann boundary condition is used over all remaining boundaries.

At the outlet, for both temperature and velocities, a convective boundary condition (Sohankar *et al.*, 1998) is applied as follows:

$$\frac{\partial \phi}{\partial t} + U_{bulk} \frac{\partial \phi}{\partial n} = 0$$

Here, ϕ stands for velocities and temperature and n is the perpendicular direction to the outlet surface.

Finally, cyclic boundary condition is used for all the flow parameters in the θ direction.

3.5 Fully Developed Flow Assessment

The criterion for starting the extraction of the statistics of the flow from the numerical simulations is the status of numerically fully developed

condition. Since the governing equations in LES simulations have elliptic form, it always takes time before the simulations reach the state of fully development. So, in order to establish whether a simulation has become fully developed, it is conventional to keep track of one of the flow parameters, e.g. friction coefficient or the Nusselt number.

In this work, fluctuations of instantaneous Nusselt number at four different heights are calculated and studied. Figure 3.3 shows two of those Nusselt numbers and their variation as a function of time. In these figures filtered values at each point are the average of 4000 neighboring samples and the average values are the arithmetical average of all samples.

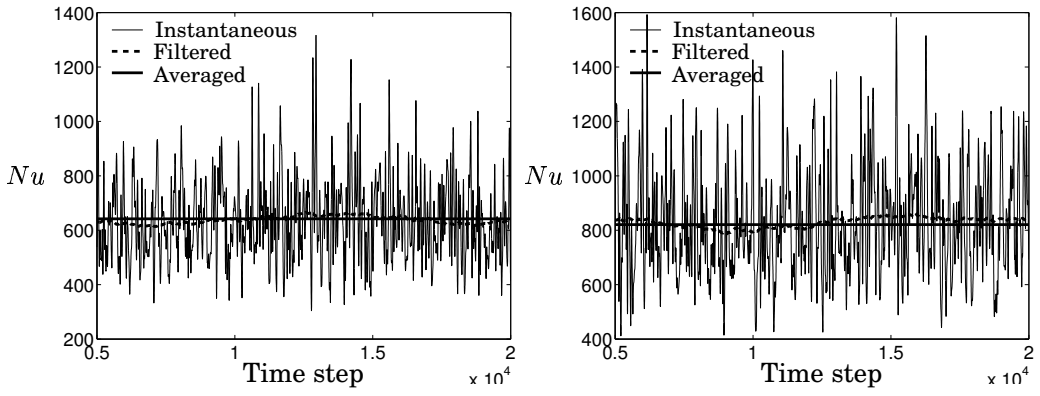

(a) At $z/H = 0.7$. (b) At $z/H = 0.9$.

Figure 3.3: Assessment of fully developed flow regarding local Nusselt number.

As can be seen, the instantaneous local Nusselt number fluctuates uniformly around the averaged value. This can be better observed by considering filtered values which are shown by dashed lines. According to this figure, in the last 20000 time steps, it can be concluded that the simulation can be considered as fully developed and the statistical parameters can be extracted from it.

Another method of investigating whether or not simulations can be considered as fully developed is to extract some statistics, preferably the most sensitive ones, from different contiguous simulations and to compare them. This is shown for the stream-wise velocity and the shear stress in Figure 3.4. In this figure, the curves are obtained from three contiguous simulations, for each of which 5000 time steps are used to extract the mean flow and turbulence parameters. It can be

observed that very little differences exist between the curves. In fact, the largest differences lie in the region close to the outer shell far from the inner hot tube which is not our concern. Again, it can be concluded that the simulated flow can be considered as fully developed for the last 15000 time steps of the simulation.

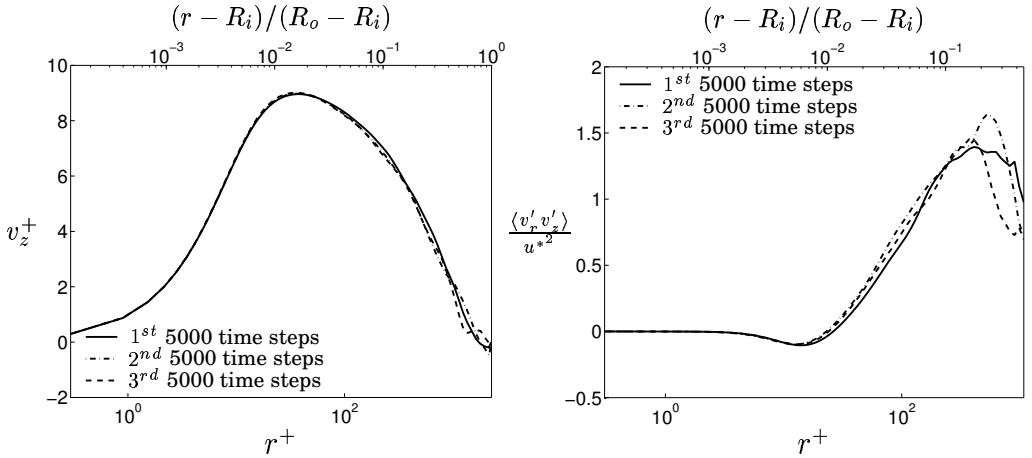

(a) Dimensionless velocity.

(b) Reynolds shear stress.

Figure 3.4: Velocity and shear stress at $z/H = 0.8, Gr = 2.9 \cdot 10^{11}$ for contiguous averaged data.

Hereafter, the mean flow and turbulence parameters and statistics are calculated using the last 15000 time steps of the simulations.

3.6 Grid and Domain Study

Obtaining grid independent results is usually an important issue in RANS simulations. The results which are obtained by such grids are called *grid independent results*.

However, for the LES method, in which the turbulence is simulated and not modeled, defining a grid independent result is rather ambiguous. This means that more accurate results can be obtained by implementing finer grids. In fact, turbulent flows consist of many different length scales from large to very small, and the finer the grid becomes, the smaller scales can be captured and consequently more accurate result can be achieved. If the smallest scale of turbulence is defined as Kolmogorov length scale, i.e. $\eta \equiv (\nu^3/\epsilon)^{1/4}$, the cells of the final grid shall have, at maximum, half of this size and that is in fact a grid which

yields DNS result. The reason for cells to have half of the Kolmogorov length is that at least two cells are needed in order to simulate an eddy.

The term *suitable* or *reliable*, in the literature, is referred to a grid for which the cut-off takes place in inertial subrange, where the energy spectra of fluctuations are proportional to $\kappa^{-5/3}$, and the stream-wise and span-wise dimensionless cell lengths and widths of the grid near the wall are $\Delta z^+ \leq 50$ and $\Delta\theta^+ \leq 15$, respectively, see e.g. Kaltenbach *et al.* (1999).

It should be mentioned that all of these grid characteristics can be examined after the simulations are performed. So it is probably worthwhile to acquire some crude information from RANS simulations before starting LES computations.

Another important aspect of a grid is its span-wise extension. For the present computations, it means that in Figure 3.1, the angle θ should be large enough to covers the largest scales of the turbulence that acquire energy of turbulence.

3.6.1 Grid Specifications

Figures 3.5(a) and 3.5(b) show the stream-wise and the span-wise variation of dimensionless wall adjacent cell sizes along the inner hot tube, respectively.

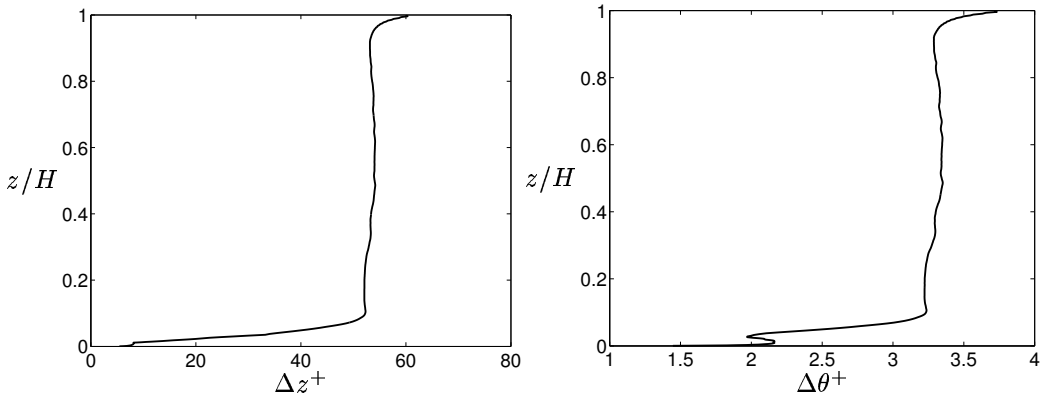

(a) Stream-wise spacing.

(b) Span-wise spacing.

Figure 3.5: Near wall spacing based on the wall units.

As can be seen, the value of Δz^+ in most part of the computational do-

main is about 50. Also, the value of $\Delta\theta^+$ for the wall adjacent cells does not become higher than 3.5. All the cells which lie at $r \leq (R_o - R_i)/2$ have a $\Delta\theta^+ \leq 15$. Regarding these values, it can be concluded that the grid spacing is suitable for performing well-resolved LES computations.

Another method, as already discussed, is to check the variation of energy spectra of fluctuations as a function of wave length. One-dimensional spectra $E_{ij}(\kappa)$ in the x_i direction are defined as to be *twice* of the one-dimensional Fourier transform of two-point correlation, R_{ij} (Pope, 2000):

$$E_{ij}(\kappa) \equiv \frac{1}{\pi} \int_{-\infty}^{\infty} R_{ij}(\mathbf{e_i} x_i) e^{-i\kappa x_i} dx_i \tag{3.9}$$

Energy spectra for velocity and temperature fluctuations in a region close to the wall are shown in Figure 3.6. For details on how the energy spectra are calculated see Appendix A. As can be seen in the figures, the cut-off has taken place well beyond the range where energy spectra are proportional to κ^{-3}. This is a region that is believed to follow immediately the inertial subrange, where $E \propto \kappa^{-5/3}$ (Peng & Davidson, 2002).

Finally, as Smagorinsky SGS viscosity depends on grid size, its magnitude can give an insight on how fine the mesh is. Figure 3.7 shows the turbulent viscosity normalized by the viscosity at different heights. It can be observed that the SGS viscosity is, at maximum, less than half of the laminar viscosity and it occurs rather far from the wall. In fact in major part of the boundary layer, this ratio remains less than 0.2. This shows again that the grid is fine enough.

From the above results, it can be concluded that the grid has almost completely fulfilled the requirements of a typical grid which is supposed to be suitable for well-resolved LES simulations.

3.6.2 Computational Geometry Extension

It is known that the effect of the computational geometry extension in the homogeneous directions (here the span-wise angle θ) on the final averaged results is very important. So, it is crucial to study the effect of different angles in order to acquire the best results which are independent of the extent of the geometry in the homogeneous directions.

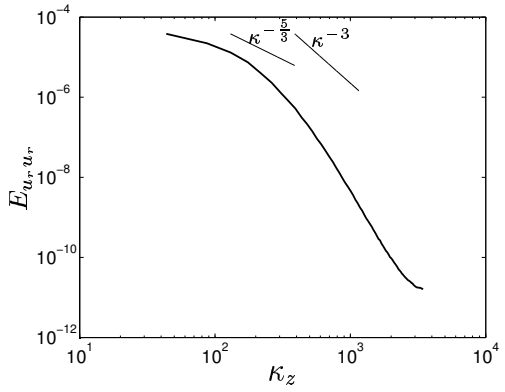

(a) Radial velocity energy spectrum.

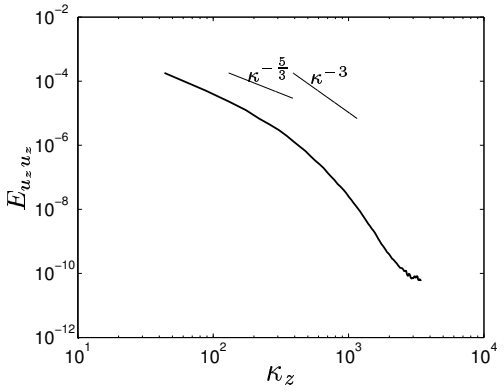

(b) Axial velocity energy spectrum.

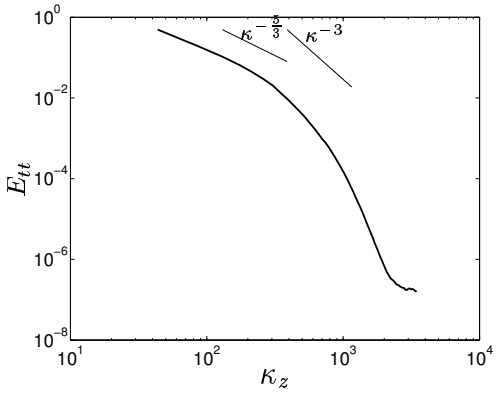

(c) Temperature energy spectrum.

Figure 3.6: One dimensional energy spectra at r^+=59, Gr_z=$1.8 \cdot 10^{11}$.

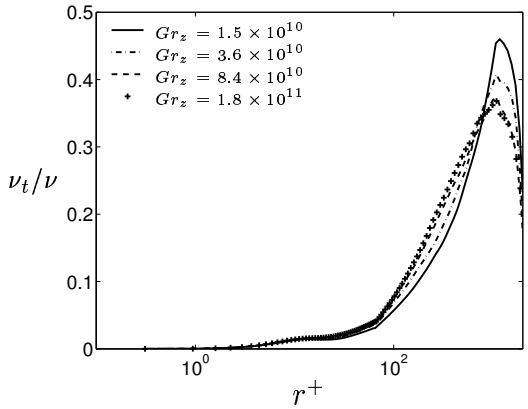

Figure 3.7: SGS viscosity variation along cylinder height.

In this study, computational geometries with different span-wise angles, $\theta = 18^o, 36^o, 54^o, 72^o$ and 90^o, are implemented and the results of mean flow velocities and Reynolds shear stresses for the three last angles are compared in Figure 3.8. Although the grid spacing in the θ-direction is the same for all grids it can be seen that the difference between the curves for $\theta = 72^o$ and $\theta = 90^o$ is less than that for $\theta = 54^o$ and $\theta = 72^o$, for both velocity and shear stress. Although it is not shown, the difference between the results of other computational geometries with $\theta = 18^o$ and $\theta = 36^o$ was even larger.

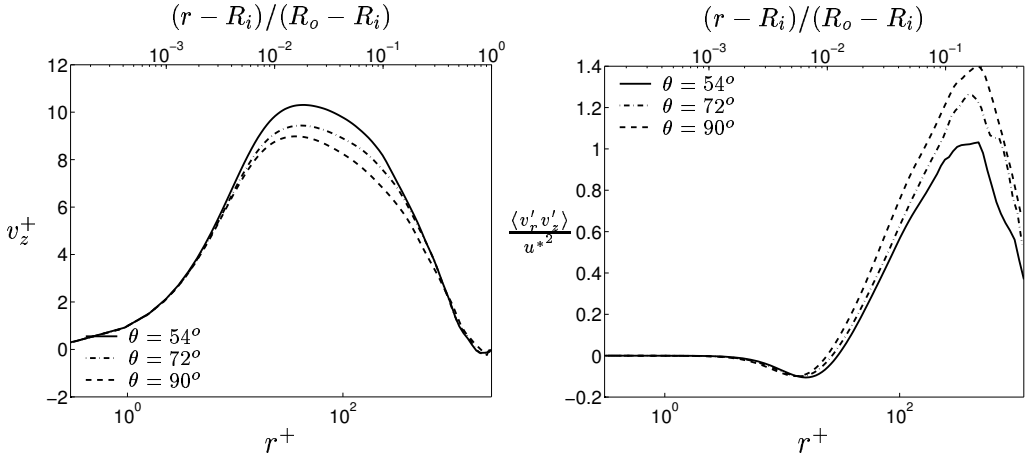

(a) Dimensionless velocity.

(b) Reynolds shear stress.

Figure 3.8: Velocity and shear stress at $z/H = 0.8, Gr_z = 2.9 \cdot 10^{11}$ for different domains.

As can be seen in Figure 3.9, the geometry with $\theta = 18^o$, yields very different Nusselt number compared to other geometries, although it is not quite clear in logarithmic plot.

From the above investigations, it can be concluded that the chosen final computational geometry with $\theta = 90^o$ has yielded results which are almost domain-independent.

Regarding the above investigations, hereafter, all the results are based on the grid-size of $n_r \times n_z \times n_\theta = 98 \times 402 \times 162$ with $\theta = 90^o$.

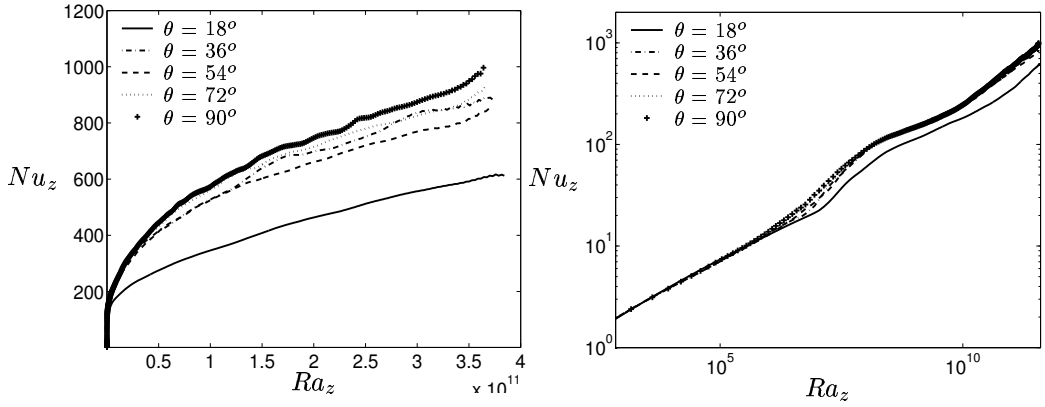

(a) Linear plot.

(b) Logarithmic plot.

Figure 3.9: Assessment of domain-independent results regarding variation of Nusselt number.

3.7 Wiggle Detection

Figure 3.10 shows the time-averaged blending factors of the Van-Leer and central difference with deferred correction schemes for velocities and temperature. In these figures, $\langle\alpha'\rangle = 0$ and $\langle\alpha'\rangle = 1$ represent pure Van-Leer and central difference with deferred correction schemes respectively. Studying the figures, it can be found that the most affected direction is the radial direction. This means that the most wiggles were detected in this direction. This is probably due to the spatial resolution of the grid in this direction which is not fine enough to eliminate wiggle generation. However, for the other two directions and the temperature variable, it can be observed that except for the inlet region, the dominant scheme is the central difference scheme. Also in the r-direction, the region close to the inner hot tube is not strongly affected by wiggles.

3.8 Mean Flow Quantities

The local Grashof number in this study reaches to $Gr_z \simeq 5 \cdot 10^{11}$ at maximum height of the geometry. However, as the upper part of the flow is affected by the outlet due to the acceleration of the flow at this region and also due to existence of recirculating flows near the outlet (see Figure 3.11(a)), the results of this part, i.e. from $Gr_z \simeq 3.7 \cdot 10^{11}$ or $z/H \simeq 0.9$, are not as reliable as the results of the rest of the domain

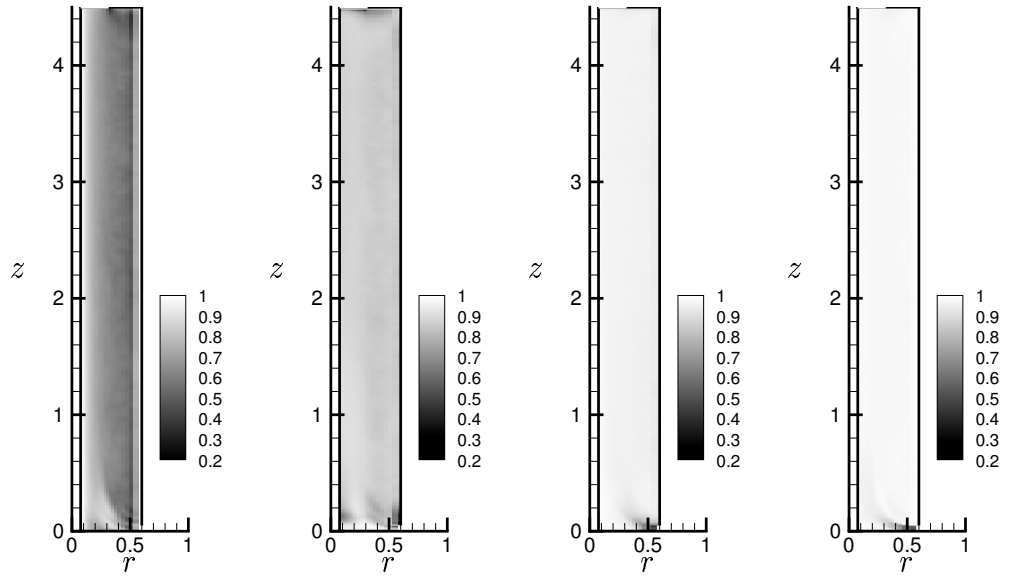

(a) $\langle \alpha'_r \rangle$. (b) $\langle \alpha'_z \rangle$. (c) $\langle \alpha'_\theta \rangle$. (d) $\langle \alpha'_t \rangle$.

Figure 3.10: Contours of time-averaged blending factor, $\langle \alpha' \rangle$.

(in sense of natural convection being dominant phenomenon) and hence are not analyzed.

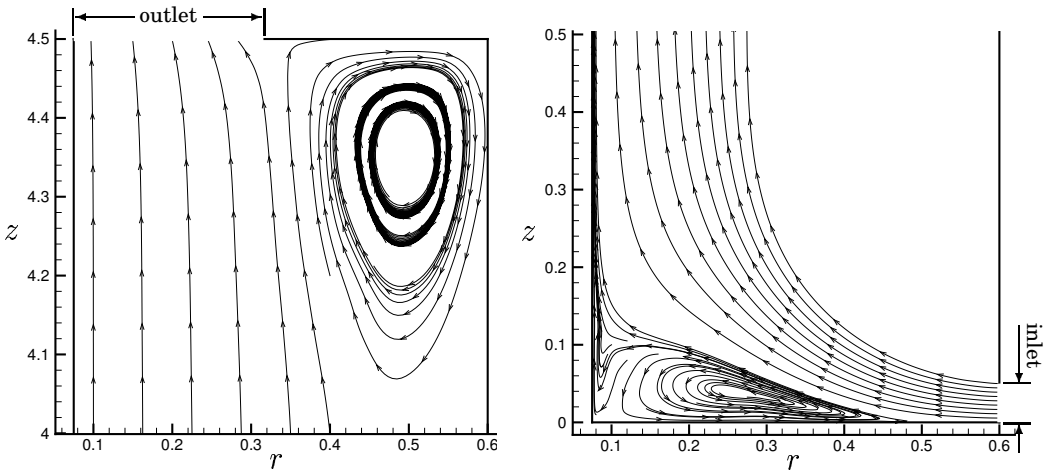

(a) Outlet region. (b) Inlet region.

Figure 3.11: Flow near the outlet and the inlet.

However these recirculating regions exist in the flow, it should be men-

tion that the effect of them compared to the natural convection boundary layer is rather weak. This can be understood by considering Figure 3.12 which shows the vector plot of the two recirculating regions of the Figure 3.11. It can be seen that the vectors of the recirculating regions are much weaker than those of the boundary layer showing that the natural convection is the dominant process.

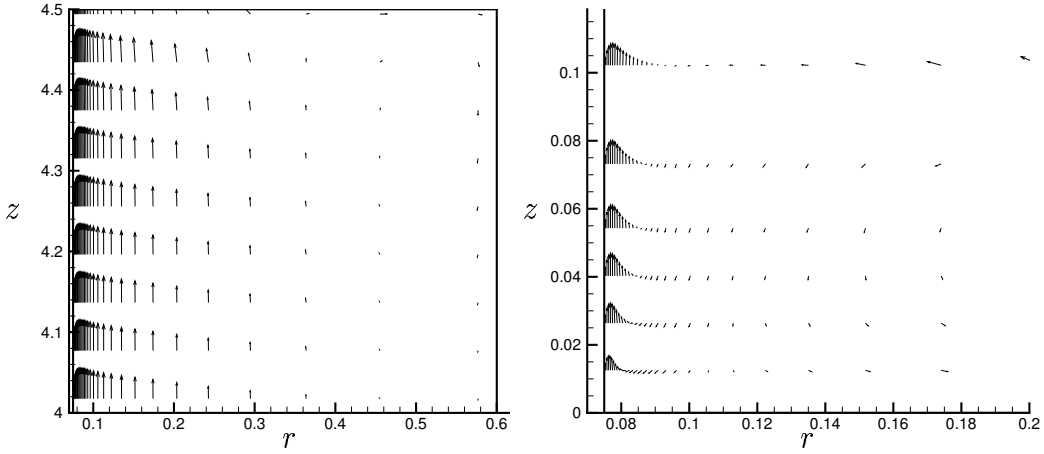

(a) Outlet region.

(b) Inlet region.

Figure 3.12: Vector plot of the flow near the outlet and the inlet.

Figure 3.13 compares the velocity and temperature profiles in the laminar region of the geometry with those obtained from similarity solution by Ostrach (1952) for a vertical flat plate. Although close to the wall the results are in complete agreement, discrepancies become larger farther from the wall. This is probably due to first the curvature of the cylinder that causes different boundary layer growth and second the existence of turbulence both at the inlet and that generated from the recirculating flow at the lower part of the cylinder (see Figure 3.11(b)) and finally incapability of Smagorinsky model to simulate the laminar flows accurately.

The effect of generated turbulence near the inlet on the commencement of turbulent boundary layer will be explained in more detail in connection to the discussion of Nusselt number variations over the inner tube.

Figure 3.14 shows the velocity and temperature profiles at different Grashof numbers. For information about how the Grashof numbers are related to cylinder height, Figure 3.15 depicts the variation of local

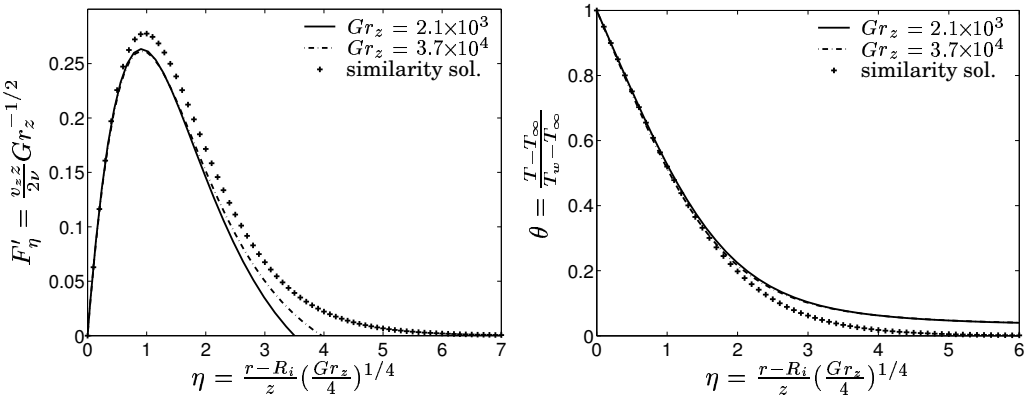

(a) Velocity profiles.

(b) Temperature profiles.

Figure 3.13: Comparison of velocity and temperature profiles with the similarity solution results in the laminar region.

Grashof number versus cylinder height. As can be seen in Figure 3.14, although the profiles of velocity collapse on each other and resemble a self-similar behavior, this is not the case for the temperature profiles. This is expected as it is known that the friction velocity makes the profiles to collapse in the inner part of the boundary layer, which is a constant heat flux layer and consist of a conductive sublayer, thermo-viscous and buoyant sublayer (George & Capp, 1979). It can be seen that this scaling is not appropriate for outer part of the thermal boundary layer. However, this problem is tackled by George & Capp (1979) and useful scalings for both the inner and the outer layer are proposed.

Figure 3.16 compares the mean flow velocity and temperature profiles obtained from LES simulations and experiments on the flat-plate and vertical cylinder at a specific Grashof number. It can be seen that although the results of the present study are in good agreement with the results of Tsuji & Nagano (1988*a*), the results of Persson & Karlsson (1996) are rather different.

As a common behavior in all graphs, however, except for a very small distance from the wall, $r^+ < 1.2$, the velocity does not follow the law of the wall, $v_z^+ = r^+$, the same way it does for forced convecting boundary layers. However, Figure 3.16(b) shows that temperature follows the law of the wall in the region $r^+ < 5$, alike forced convecting flows.

Figure 3.17 shows variation of Nusselt number as a function of Rayleigh number. Compared to the results of Tsuji & Nagano (1988*a*) and pro-

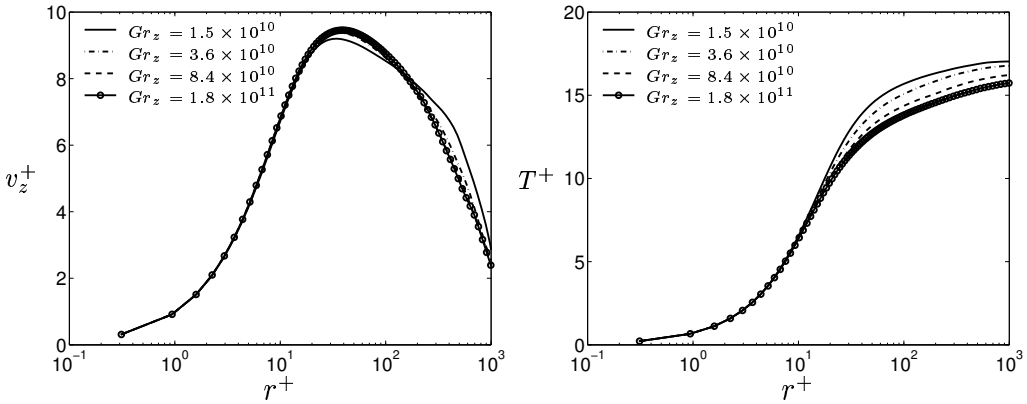

(a) Dimensionless velocity.

(b) Dimensionless temperature.

Figure 3.14: Mean velocity and temperature profiles.

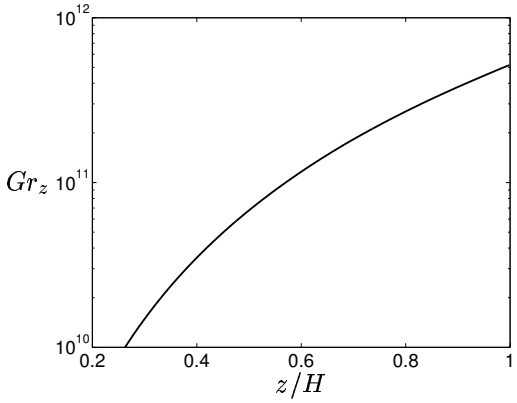

Figure 3.15: Local Grashof number variation versus cylinder height.

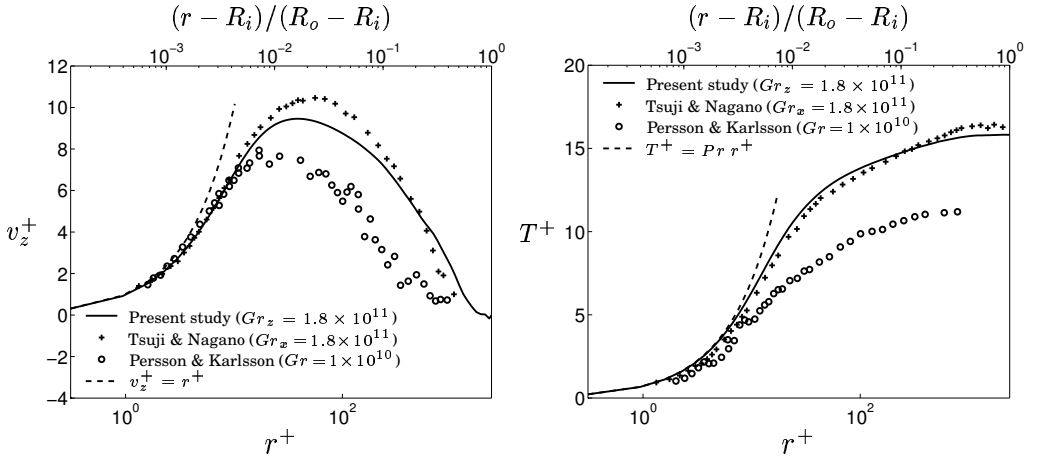

(a) Dimensionless velocity.

(b) Dimensionless temperature.

Figure 3.16: Comparison of stream-wise velocity and temperature with experimental data.

posed correlation for the laminar region, there is a very good agreement for both the laminar and the turbulent region. However, the major difference is in the transition region. The transition for the studied flow seems to be starting from $Ra_z = 10^6$ compared to the flow along the flat plate for which transition starts from $Ra = 8 \cdot 10^8$. The difference is probably due to first the turbulent inlet boundary condition, second, inherent difference between characteristics of boundary layer along a vertical flat plat and a vertical slender cylinder and third, existence of the outer shell which embraces the whole cylinder and provokes instabilities by creating some recirculating flows in the proximity of boundary layer.

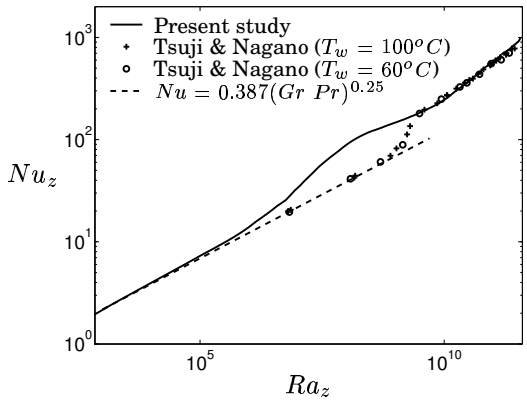

Figure 3.17: Nusselt number as a function of Rayleigh number.

Another difference in Figure 3.17 is the overshoot of the predicted Nusselt number in the commencement of turbulent boundary layer which was not observed by Tsuji & Nagano (1988*a*) but has been mentioned in previous experimental investigations (e.g. Cheesewright, 1968).

3.9 Turbulence Quantities

Mean flow quantities can not give enough information about turbulent characteristics of the flow. So, in order to study the turbulence in a flow, it is very important to extract turbulence quantities, which are sometimes referred to as *turbulence statistics*, and analyze them.

Among turbulence quantities, the integral time scale is one of the most important quantities from an experimentalist view point. It is defined as the half of a minimum time interval between two contiguous signals which is needed to keep them uncorrelated. Mathematically, this time is twice of the area below the autocorrelation curve. Autocorrelation for a set of data with constant time interval, $\Delta\tau$, is defined as:

$$R_j^{\phi}(j\Delta\tau) = \frac{\sum_{i=1}^{N-j} \phi_i' \phi_{i+j}'}{N-j}, \quad j = [0..N-1] \tag{3.10}$$

Correspondingly, the integral time scale for a variable ϕ, is defined as the area below the autocorrelation curve, as follows:

$$T_{int}^{\phi} = \int \frac{R_j^{\phi}}{R_0^{\phi}} d\tau \tag{3.11}$$

Autocorrelation curves for the stream-wise velocity and temperature are shown in Figures 3.18(a) and 3.18(b), respectively. It can be found that the maximum integral time scale for stream-wise velocity and temperature autocorrelation curves are $T_{int}^{v_z} = 0.15sec$ and $T_{int}^{t} = 0.07sec$, respectively. In non-dimensional form these times correspond to $T^{v_z} u^*/r_{max} = 1.33$ and 0.62. For estimating the integral time scales, the time extension has been supposed to be from zero to where the curves cross the time axes for the first time. These estimated times suggest that for obtaining uncorrelated data, the minimum time interval between each two contiguous samples should be $0.3sec$ (2.66 in dimensionless form).

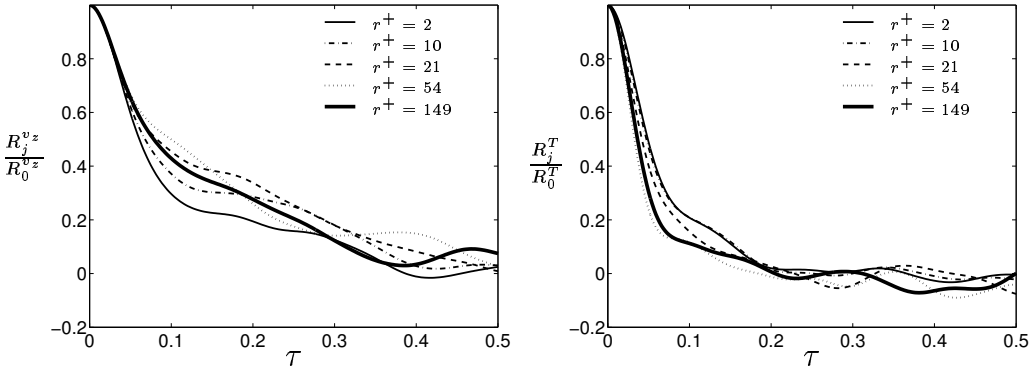

(a) v_z autocorrelation curve.

(b) Temperature autocorrelation curve.

Figure 3.18: Autocorrelation curves at $Gr_z = 2.1 \cdot 10^{11}$.

Reynolds stresses, which consist of normal and shear stresses, and turbulent heat fluxes are other important turbulence parameters. The Reynolds shear stress is very important from the point of view that it mostly contributes to the process of mixing which is very important in a turbulent flow. Normal stresses are also very important in the sense that they contribute in production and dissipation of energy for Reynolds shear stress and vice versa. So, a correct distribution of these stresses is vital for predicting and studying a turbulent flow.

Comparison of normalized predicted resolved stream-wise normal stress, $\sqrt{\overline{v_z'v_z'}}/u^*$, wall-normal stress, $\sqrt{\overline{v_r'v_r'}}/u^*$ and temperature fluctuations, $\sqrt{\overline{t't'}}/t^*$, with those measured by Tsuji & Nagano (1988*b*) and Persson & Karlsson (1996) is shown in Figure 3.19. As can be seen, temperature fluctuations get the largest peaks for both simulation and the experiment performed by Tsuji & Nagano (1988*b*). However, this is not the case for Persson & Karlsson (1996) experiment in which the stream-wise normal stress has the largest peak. A comparison between present work and Tsuji & Nagano (1988*b*) results shows that velocity and temperature fluctuations are qualitatively in good agreement and the location of the peaks almost match each other. However, predicted temperature fluctuations are almost always larger than the experimentally measured values. Also, no constant value region such as that observed for $\sqrt{\overline{v_r'^2}}/u^*$ in the experiment, in the region $7.5 < r^+ < 40$, can be observed in the LES-simulation.

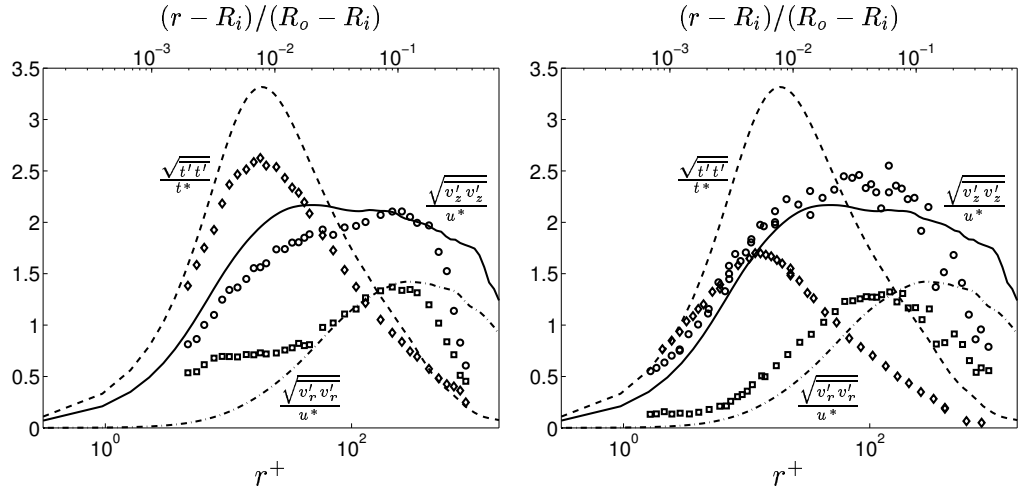

(a) Experimental data from Tsuji & Nagano (1988*a*), $Gr_x = 8.99 \cdot 10^{10}$.

(b) Experimental data from Persson & Karlsson (1996), $Gr = 1 \cdot 10^{10}$.

Figure 3.19: Normal stresses and temperature fluctuations. Lines: simulation, $Gr_z = 8.9 \cdot 10^{10}$; markers: experiments.

As can be seen in Figure 3.19(b), descripancies between simulation and experimental results presented by Persson & Karlsson (1996) are even larger. The location of the peaks in the experimental results except for stream-wise normal stress, are closer to the wall compared to those of the simulation. Although the measured wall-normal stress shows almost the same behavior as the computed one, which is contradictory to the measurements of the Tsuji & Nagano (1988*b*), still it shows no tendency to become zero quite close to the wall.

Figure 3.20 compares the normalized resolved shear stress, $\overline{v_r' v_z'}/u^{*2}$, stream-wise turbulent heat flux, $\overline{v_z' t'}/u^* t^*$ and wall-normal turbulent heat flux, $\overline{v_r' t'}/u^* t^*$ again with measured values by Persson & Karlsson (1996) and Tsuji & Nagano (1988*b*).

As can be seen in Figure 3.20(a), the wall-normal heat flux is almost in perfect agreement with the measured values. Stream-wise heat flux and Reynolds shear stress are also qualitatively in agreement with measurements and the location of the maxima match each other fairly well. Although both measurement and simulation show that shear stress becomes zero near the wall in the region $r^+ < 4$, the existence of a region with negative shear stress is not confirmed by measurements whereas it exist in the simulation. The existence of such a negative region for Reynolds shear stress not only can be seen in measurements of Persson & Karlsson (1996) in Figure 3.20(b) but also it is reported

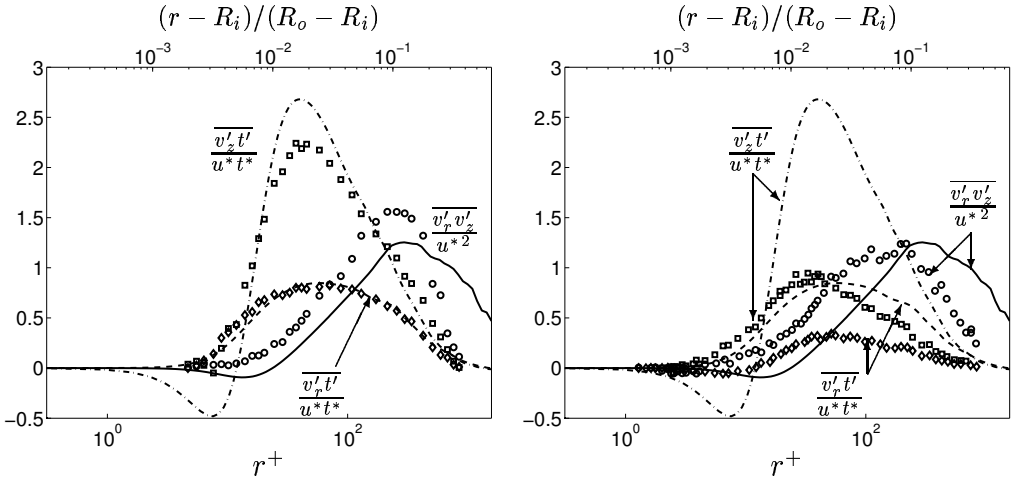

(a) Experimental data from Tsuji & Nagano (1988*a*), $Gr_x = 8.99 \cdot 10^{10}$.

(b) Experimental data from Persson & Karlsson (1996), $Gr = 2 \cdot 10^{10}$.

Figure 3.20: Turbulent shear stress and heat fluxes. Lines: simulation, $Gr_z = 8.9 \cdot 10^{10}$; markers: experiments.

previously by Miyamoto *et al.* (1982) and Cheesewright & Ierokipiotis (1984).

For the shear stress and the heat fluxes, discrepancies between simulation and measurements in Figure 3.20(b) are quite large. Contrary to the simulation and the results of Tsuji & Nagano (1988*b*), the peak of normalized shear stress is larger than those of the stream-wise and wall-normal turbulent heat fluxes. Also, a negative region for the measured wall-normal heat flux exist which can be observed neither in the simulation nor in the Tsuji & Nagano (1988*b*) measurements. On the contrary, however, the negative stream-wise heat flux region that was confirmed by both simulation and Tsuji & Nagano (1988*b*) measurements, can not be observed in Persson & Karlsson (1996) results.

Knowing the analytical behavior of turbulence quantities, it is useful to compare the measurements versus simulation to examine the credibility of the obtained results. For example the cross correlation coefficient is defined as:

$$R_{uv} = \frac{\overline{v_r' v_z'}}{\sqrt{\overline{v_r'^2}} \times \sqrt{\overline{v_z'^2}}} \tag{3.12}$$

From the Taylor expansion, and by applying no slip boundary condition

and considering continuity equation, it can be found that close to the wall when r approaches zero:

$$\begin{cases} \overline{v_r' v_z'} = \mathcal{O}(r^3) \\ \overline{v_r' v_r'} = \mathcal{O}(r^4) \\ \overline{v_z' v_z'} = \mathcal{O}(r^2) \end{cases} \tag{3.13}$$

Considering equations 3.12 and 3.13, it can be deduced that R_{uv} converges to a constant as r approaches zero.

Figure 3.21 compares the cross correlation coefficient for the measurements of Tsuji & Nagano (1988*b*), Persson & Karlsson (1996) and the present simulation. It can be seen that this coefficient approaches constant values $R_{uv} \approx -0.3$ and $R_{uv} \approx -0.09$ for the simulation and Persson & Karlsson (1996) measurements, respectively. However, as this coefficient becomes zero for the measurements of Tsuji & Nagano (1988*b*), it can be deduced that the measured stresses in this experiment are not reliable in the region close to the wall.

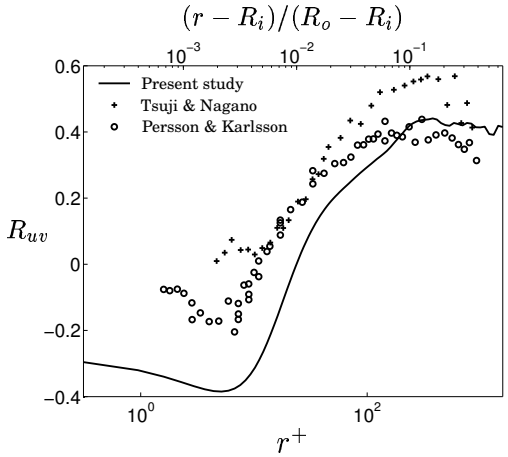

Figure 3.21: Cross correlation coefficient comparison.

3.10 Conclusions

Near wall behavior of turbulent natural convection depends on the turbulence quantities near the wall. In a buoyancy-aided vertically oriented flow near a hot object, with the onset of buoyancy influence, the flow accelerates. This causes the advection, which directly depends on velocity of the fluid near the wall, to increase. Nevertheless, it is observed that the heat transfer process is not as effective as it is in case

of pure forced convection. This is due to the process of mixing in a turbulent flow which depends on turbulent diffusion. The mixing process in a flow is highly dependent on the shear stress. In case of a natural convecting boundary layer, as it was observed in the previous section, the turbulent shear stress near the wall is almost zero. In a mixed convection process compared to a case with forced convection, $|\overline{u'v'}|$ is reduced. Consequently, in buoyancy aided flows, the turbulence production which is defined as:

$$P_k = -\rho\overline{u'v'}\frac{\partial\overline{u}}{\partial y}$$

is decreased and the diffusion of heat by turbulence is adversely affected. However, an interesting part is the region that follows the zero shear stress region. Whether a negative shear stress region follows this zero region or not is a matter of confusion. In this study and many other experiments as mentioned previously, this region with negative shear stress can be observed. While some other experiments like the one performed by Tsuji & Nagano (1988*b*) deny the existence of such a region. It is difficult to say that the negative shear stress region in the present work exists naturally or it is created due to the existence of mixed convection. Nevertheless, it is obvious that the natural convection is the dominant process in this study. And also, the credibility of both experiments, i.e. Tsuji & Nagano (1988*b*) and Persson & Karlsson (1996), near the wall is under question. The constant wall-normal stress region reported by Tsuji & Nagano (1988*b*) may simply be due to experimental errors. Also, contradictory results of Persson & Karlsson (1996) with respect to the present work and other experiments suggest both inaccurate near-wall results and/or miscalculations in friction temperature, t^*.

Despite all of the contradictions between the present work and experiments, it can be deduced that the turbulent natural convection boundary layer has a unique structure which is different from other turbulent structures observed in the nature. So, a further study of this problem both experimentally and numerically is highly desirable.

Chapter 4

Direct Numerical Simulation

In order to capture the details of the structure of a turbulent flow, Direct Numerical Simulation (DNS) is the best and the most powerful tool which is available beside experimental tools. In this method even the small scales of turbulence should be simulated. It means that a very fine mesh whose size is in the range of Kolmogorov micro-scales should be implemented. The drawback with this method is that it needs very powerful computers with high memory capacities even for very simple geometries and flows.

DNS of fully developed natural convection in a vertical channel was studied recently (see e.g. Versteegh & Nieuwstadt (1998) and Davidson *et al.* (2003)) and interesting results have been published. This problem has a very simple geometry and at the same time a complicated flow. In the previous chapter, natural convection boundary layers were studied. The difference between a channel flow and a boundary layer flow however is that in fully developed channel flow, the mean flow and turbulence properties do not change in the direction of the flow while this happens in case of boundary layer flow.

Unfortunately, from the previous investigations (see e.g. Versteegh & Nieuwstadt (1998) and Peng & Davidson (2002)), it is found that the accuracy of the results is very much dependent on the channel height. To investigate this, the DNS of the natural convection in a vertical channel with differentially heated walls for three different channel heights has been studied and results are compared.

4.1 Governing equations

The governing equations for this problem are three dimensional continuity, Navier-Stokes and energy equations in the Cartesian coordinate system. The adopted geometry is depicted in figure 4.1.

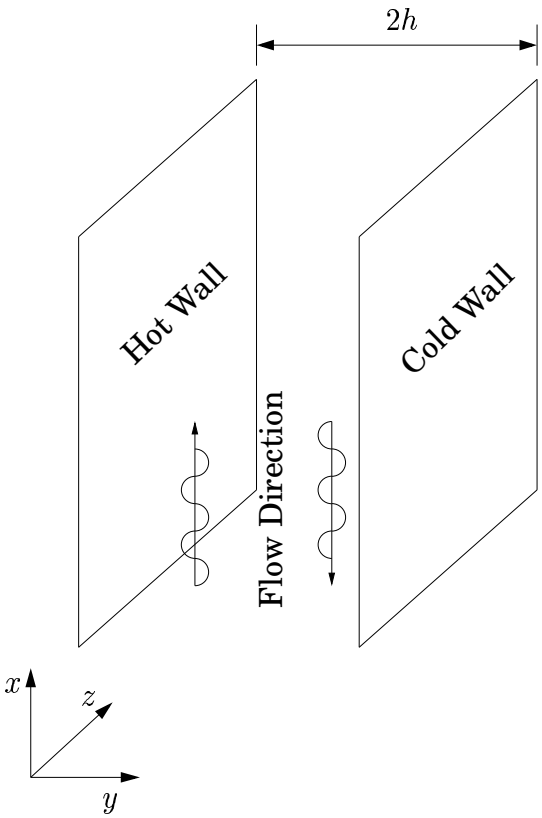

Figure 4.1: Channel flow geometry.

The set of equations in non-dimensional form reads:

$$\frac{\partial u_j}{\partial x_j} = 0 \tag{4.1}$$

$$\frac{\partial u_i}{\partial t} + \frac{\partial}{\partial x_j}\left(u_j u_i\right) = -\frac{1}{\rho}\frac{\partial p}{\partial x_i} + \nu\frac{\partial^2 u_i}{\partial x_j \partial x_j} + \frac{Gr\ \nu^2}{(T_h - T_c)(2h)^3}(T - T_f)\delta_{1i} \tag{4.2}$$

$$\frac{\partial T}{\partial t} + \frac{\partial}{\partial x_j}\left(u_j T\right) = \frac{\nu}{Pr}\frac{\partial^2 T}{\partial x_j \partial x_j} \tag{4.3}$$

In which:

$$\nu = 1/150$$

$$T_h = 1,\ T_c = 0$$

$$Pr = 0.7$$

$$h = 1$$

$$\Delta T = T_h - T_c$$

$$Gr = g\beta\Delta T(2h)^3/\nu^2 = 9.6 \times 10^5$$

The three different geometries which have been used for numerical calculations have dimensions of $7.6\pi \times 2 \times 2\pi$, $12\pi \times 2 \times 2\pi$ and $18\pi \times 2 \times 2\pi$ in the x, y and z directions, respectively. Cyclic boundary condition is applied both in the x and z directions.

4.2 Numerical Method

The governing equations are solved using a conventional finite volume method (Versteegh & Malalasekera, 1995). As the least dissipative and at the same time most practical scheme is central difference scheme, it is used to discretize the equations in space. In time, the second-order Crank-Nicolson scheme is used for discretization. The numerical procedure is based on an implicit, fractional step technique with a multigrid pressure Poisson solver (Emvin, 1997) and a non-staggered grid arrangement (Davidson & Peng, 2003).

4.3 Results

Three different geometries with different channel lengths in the x-direction ($L = 7.6\pi, 12\pi$ and 18π) are studied. In each case the same 66×66 mesh in the y and z-directions with a 7-percent stretch along the y (wall normal direction) is used. In the x-direction (stream-wise direction) $82, 130$ and 194 nodes are used. In all of the above grid configurations, the stream-wise and the span-wise dimensionless grid lengths are approximately $\Delta x^+ = 20$ and $\Delta z^+ = 6.5$, respectively.

To check the location of cut-off and therefore the validity of DNS simulation, figure 4.2 shows the result of one-dimensional energy spectrum

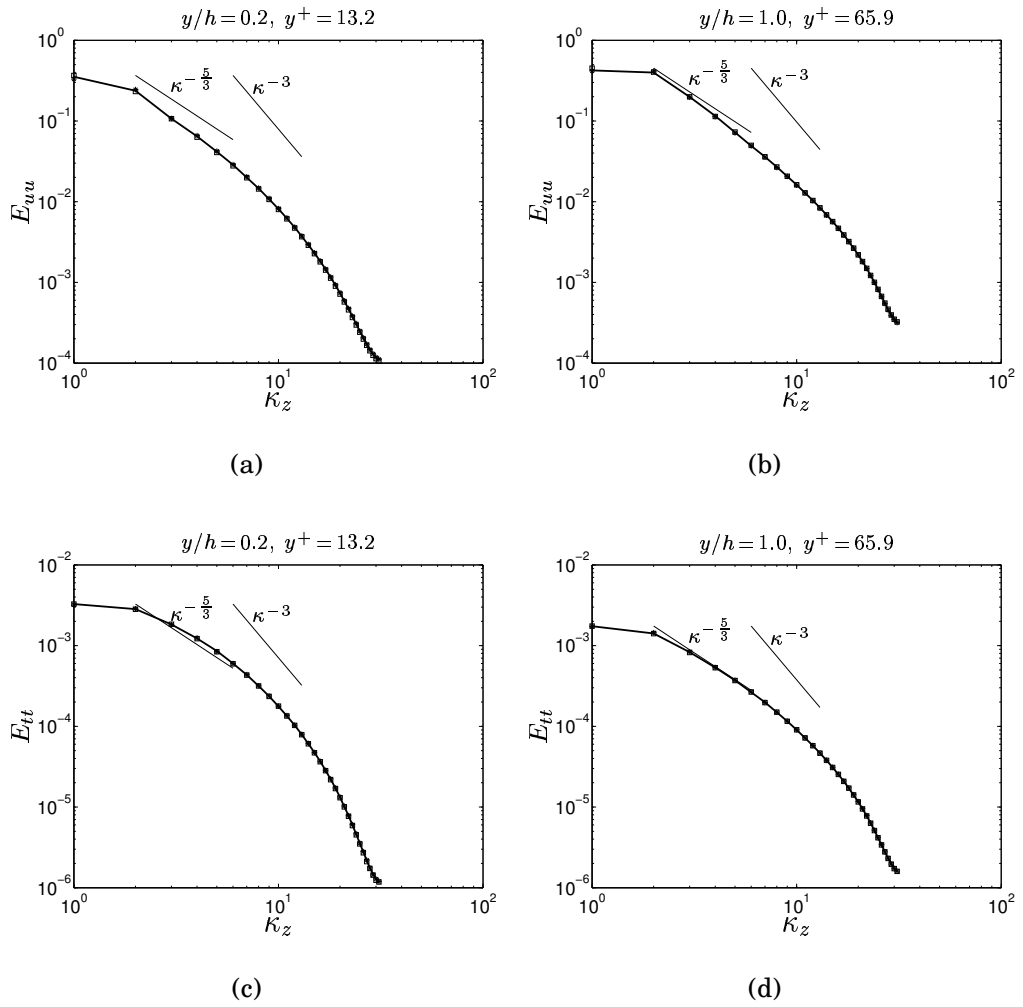

Figure 4.2: One dimensional energy spectra. Solid lines: $L = 7.6\pi$; squares: $L = 12\pi$; asterisks: $L = 18\pi$.

for both stream-wise velocity and temperature fluctuations at a location near the wall and in the middle of the channel.

As it can be observed from the figures, all three lines almost perfectly match each other. The cut-off is taken place well beyond the inertial subrange where the energy spectrum is proportional to $\kappa^{-5/3}$. This region is very small due to the low Gr-number. For buoyancy dominant thermal flows, it is believed that the inertial subrange is followed by a so-called buoyancy subrange where the energy proportionality to wave number is κ^{-3} (Kotsovinos (1991) and Peng & Davidson (2002)). Turbulence is considered to be rather isotropic at these large wave numbers.

The mean velocity and temperature profiles for three geometries are shown in figure 4.3.

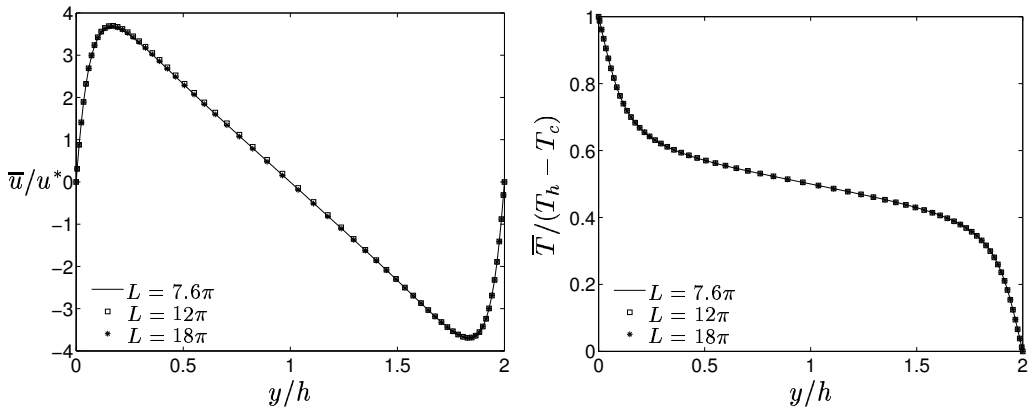

(a) Velocity profile.

(b) Temperature profile.

Figure 4.3: Mean profiles.

As can be seen, no significant difference can be observed. An inspection of velocity profile confirms the almost perfect antisymmetric behavior.

Normal and shear stresses are shown in figures 4.4(a) and 4.4(b), respectively. Ignoring very small differences between stream-wise normal stresses, all stresses are reasonably in a very good agreement with each other.

The difference between forced and natural convecting flows can clearly be seen in the shear stress behavior. In channel flow with forced convection, shear stress gets its maximum value near the wall and zero value at the center of the channel. However, in the channel flow with

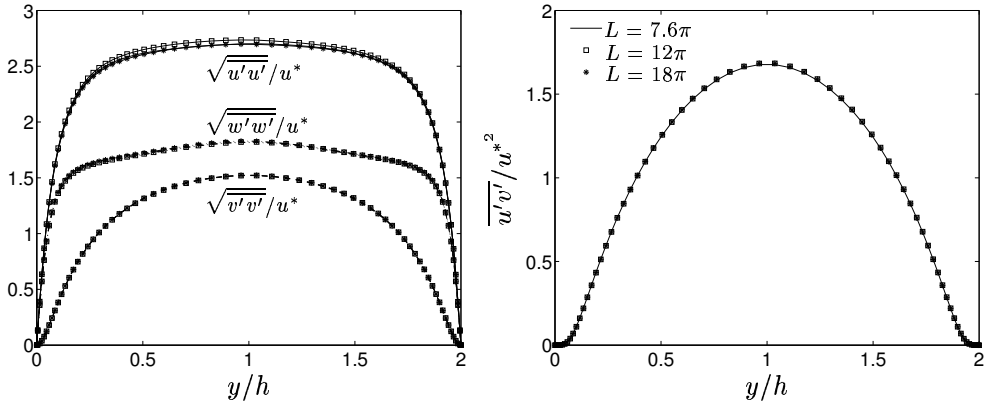

(a) Normal stresses.

(b) Shear stress.

Figure 4.4: Normalized resolved stresses.

mixed or natural convection, buoyancy term influences the shear stress in such a way that it takes the maximum value at the center in case of pure natural convecting flow. In case of mixed convection, the shear stress becomes smaller near the hot wall and larger near the cold wall (Davidson *et al.*, 2003).

Figures 4.5(a) and 4.5(b) show the turbulent heat fluxes and temperature fluctuations, respectively. Again no significant difference can be observed between the results of the three different geometries. The DNS gives a stream-wise turbulent heat flux which is much larger than the wall-normal turbulent heat flux although the stream-wise gradient of the mean temperature is zero. It should be noted that any linear eddy-viscosity RANS model would give a zero stream-wise turbulent heat flux, $\overline{u't'} = 0$, in this situation.

Near wall quantities of the present channel flow are summarized in Table 4.1. It is interesting to notice that although the wall shear stress has decreased in the present work, the wall-normal heat flux has increased. However, comparing the results of Davidson *et al.* (2003) it can be found that whenever the wall shear stress has decreased, the wall-normal heat flux has also decreased.

Performing DNS of mixed convection in a vertical channel, Davidson *et al.* (2003) noticed that unless a long channel was used, no fully developed conditions could be obtained. Considering the different behavior of the bulk velocities in the channels with different lengths (see figure 4.6) a question arises whether the difference in amplitude of fluc-

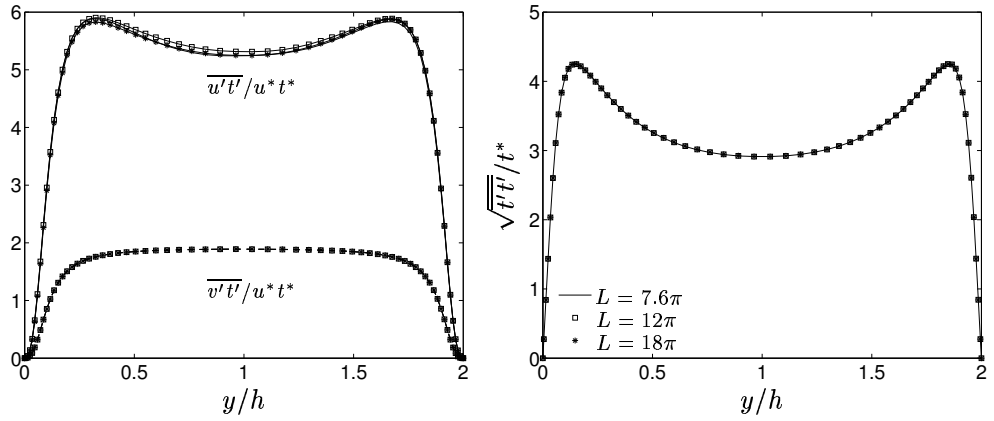

(a) Turbulent heat fluxes.

(b) Temperature fluctuation.

Figure 4.5: Resolved turbulent heat fluxes and temperature fluctuations.

	Present work $Gr = 9.6 \cdot 10^5$	Davidson *et al.* $Gr = 0$	Davidson *et al.* $Gr = 7.68 \cdot 10^6$	Kasagi & Iida $Gr = 0$
$\tau_{w,y=0}$	0.21	1	0.708	1
$\tau_{w,y=2h}$	0.21	1	0.419	1
x_{max}	18π	4π	8π	5π
U_b	0	15.6	9.8	15.2
u^*	0.46	1	0.75	1
y^+_{min}	0.3	0.4	0.2	
$(\partial T/\partial y)_w$	2.76	2.69	2.31	2.54

Table 4.1: Near wall mean flow quantities.

tuating bulk velocity will cause different turbulent stresses and heat fluxes. This would mean that the simulations are dependent on the extent of the computational domain.

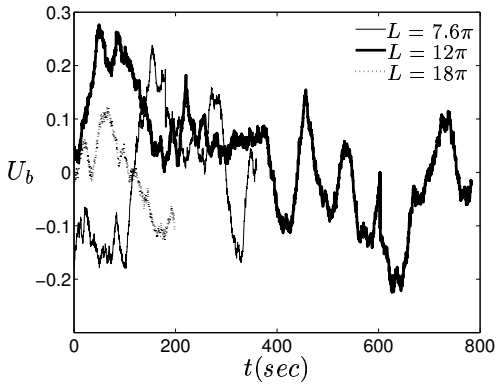

Figure 4.6: Bulk velocity.

In figure 4.6, the horizontal axis is time. The reason for having different simulation times for different geometries is that the criterion for stopping the simulations was the achievement of a reasonably antisymmetric velocity profile across the channel. It can be seen that the geometry with $L = 12\pi$ has taken the longest time to yield an antisymmetric profile compared to the other two geometries.

Comparing the results of the turbulent stresses and heat fluxes (Figures 4.4 and 4.5), it can be seen that the results are reasonably independent of geometry.

Figure 4.7(a) shows the correlation between turbulent shear stress and velocity gradient and figure 4.7(b) shows the correlation between wall normal turbulent heat flux and temperature gradient. From figure 4.7(a), it can be found that near the wall (at $y^+ < 20$) there is a discontinuity in the velocity gradient and shear stress correlation. Discontinuity comes from the sign change of the velocity gradient near the wall while the sign of the shear stress remains unchanged. This is one reason why eddy viscosity models are inadequate to model natural convection flows. In that case, models that calculate shear stress exactly, such as conventional Reynolds Stress Models (RSM), should be used.

Although the eddy-viscosity assumption for the stress-strain relation gives a negative turbulent viscosity, this is not the case for temperature gradient and wall normal turbulent heat flux relation. The turbulent Prandtl number as it is shown in figure 4.8 gets a value close to $Pr_t = 0.9$ in the $y^+ > 30$ region.

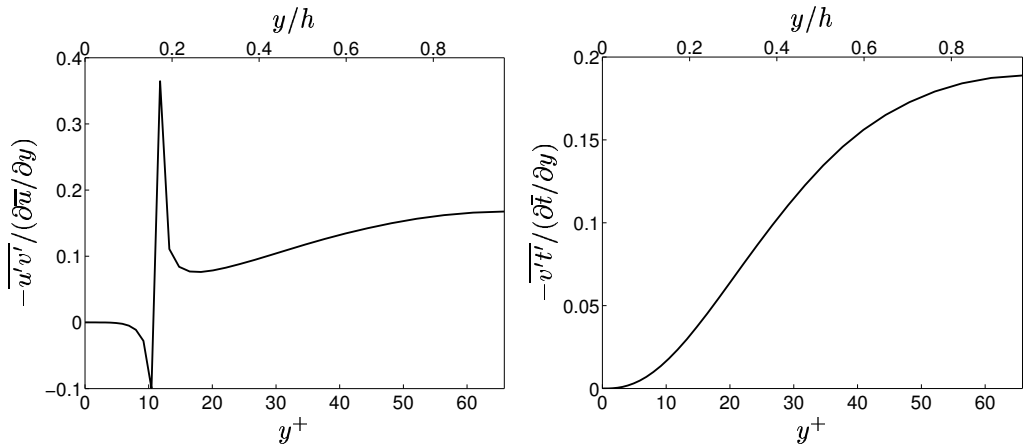

(a) Velocity gradient and shear stress correlation.

(b) Temperature gradient and turbulent heat flux correlation.

Figure 4.7: Correlations between mean flow gradients and turbulent fluctuations.

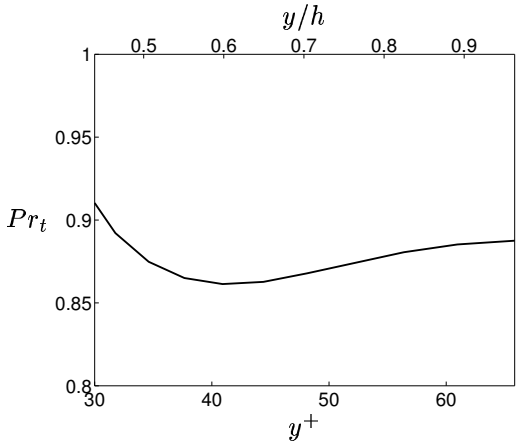

Figure 4.8: Turbulent Prandtl number.

Finally, it should be mentioned that the behavior of the studied channel flow in this investigation, is very much alike the behavior of boundary layer theory investigations over a flat plate which has been carried out by Tsuji & Nagano (1988*b*).

Chapter 5

Discussions

In the present work, two different natural convection boundary layers have been studied. These two are *natural convection boundary layer on a vertical cylinder* and *natural convection boundary layer in a differentially heated vertical channel*. The latter is different compared to the former one in the sense that there is no temperature gradient in the stream-wise direction. Another difference is that the boundary layer in the channel is fully developed and therefore it has a constant thickness. Nevertheless, there are many similar characteristics between these turbulent flows.

Figure 5.1 compares the two boundary layers, which have been numerically studied, with the experimental results of Tsuji & Nagano (1988*b*). Here, two new dimensionless transverse coordinates have been used, because r^+ is no longer suitable since the maximum of r^+ in case of the vertical channel is approximately 135. Also it was found that the maximum velocity is a better quantity for normalizing the velocity. It can be seen that these set of normalizing variables are working quite well in the inner part of the boundary layer, i.e. from wall to the location of maximum velocity. However, the result of vertical channel does not follow the other curves in Figure 5.1(a).

Figure 5.2 compares the normalized temperature variations of the three boundary layers. Here, T_{ref} stands for a temperature reference which is ambient or inlet temperature in case of Tsuji & Nagano (1988*b*) experiment and LES computations, respectively, and film temperature $T_f = 0.5$ in case of DNS computations. Contrary to the previous figure, it can be seen that in Figure 5.2(a) the profiles match each other very well in the inner part of the boundary layer where $\zeta < 1.5$.

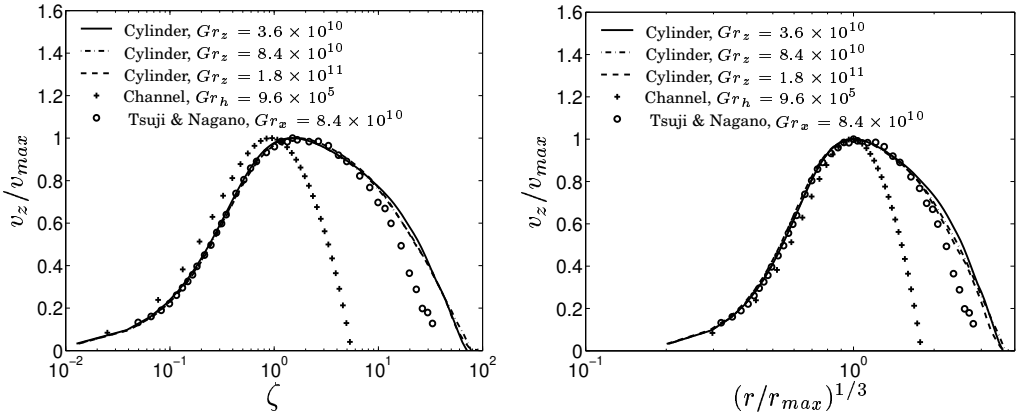

(a) (b)

Figure 5.1: Comparison of the three boundary layer velocity profiles.

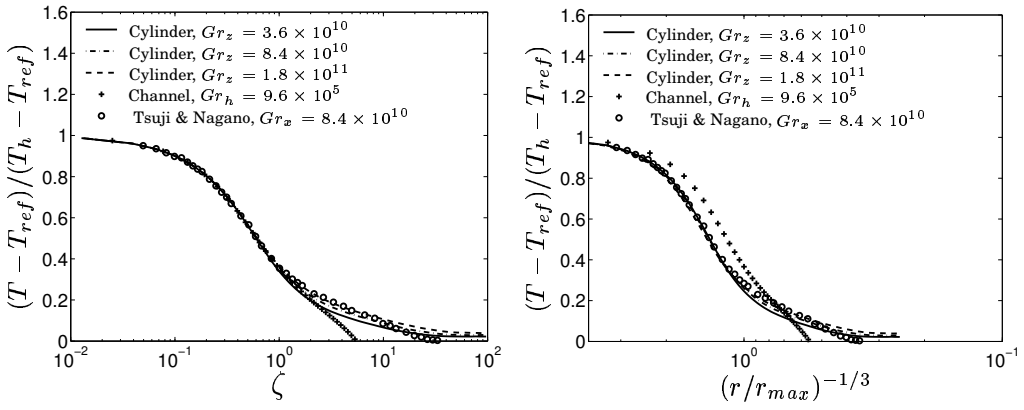

(a) (b)

Figure 5.2: Comparison of the three boundary layer temperature profiles.

Although v_{max} and $(T_h - T_{ref})$ seemed to be suitable normalizing variables for the mean flow parameters, it was found that u^* and t^* work better in case of turbulence parameters. Figure 5.3 compares the normal stresses and temperature fluctuations that are achieved by DNS and LES simulations. All the fluctuations of the vertical channel have a larger magnitude in the whole of the domain compared to those obtained by LES simulation of the vertical cylinder. The Grashof numbers based on the location of the maximum velocity and temperature at this point are $Gr_{v_{max}} = g\beta(T_h - T_{v_{max}})r_{max}^3/\nu^2 = 2.5 \cdot 10^3$ and $2 \cdot 10^2$ in case of the vertical cylinder and the vertical channel, respectively. Also at this height the Reynolds numbers based on the maximum mean flow parameters are $Re_{v_{max}} = v_{max}r_{max}/\nu = 348$ and 43 for the vertical cylinder and vertical channel, respectively.

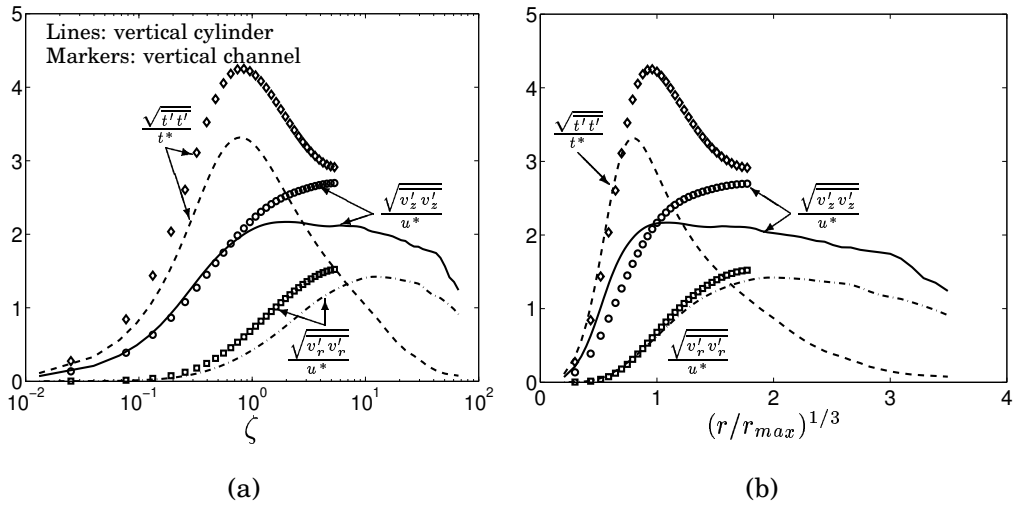

Figure 5.3: Comparison of the normal stresses and temperature fluctuations of the vertical channel ($Gr_h = 9.6 \cdot 10^5$) and the vertical cylinder ($Gr_z = 8.9 \cdot 10^{10}$).

Although there seems to be good agreement between the locations of the fluctuations maxima in Figure 5.3, from Figure 5.3(b) it can be seen that there is difference between the location of the maximum streamwise velocity fluctuations of the two boundary layers. The stream-wise normal stress of the vertical cylinder has an almost constant value over a wide range from the location of the maximum velocity to the location where $(r/r_{max})^{1/3} \approx 2$. Figure 5.4 compares the results of vertical cylinder and those presented by Tsuji & Nagano (1988*b*). Similar to the vertical channel and vertical cylinder, the maximum of the temperature fluctuations lie in the inner part of the boundary layer close to

the maximum stream-wise velocity and the maxima of all wall-normal stresses lie in the outer part of the boundary layer.

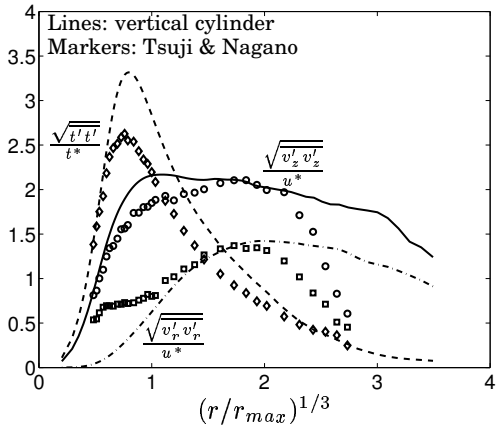

Figure 5.4: Comparison of the normal stresses and temperature fluctuations of the vertical flat plate ($Gr_x = 8.99 \cdot 10^{10}$) and the vertical cylinder ($Gr_z = 8.9 \cdot 10^{10}$).

The maximum of the temperature fluctuations in all of the above cases lies on the location where the production of $\overline{t't'}$, i.e. $-2\overline{v_r't'}\partial\overline{T}/\partial r$, is maximum. As temperature profiles and wall normal turbulent heat fluxes ($\overline{v_r't'}$) are in good agreement in all of the three boundary layers, so is the location of the temperatures fluctuations maxima. However, in case of the stream-wise normal stress, $\overline{v_z'v_z'}$, the production term in case of the vertical cylinder behaves differently compared to the other two boundary layers. The production of stream-wise normal stress is defined as:

$$P_{\overline{v_z'v_z'}} = -2\overline{v_r'v_z'}\frac{\partial\overline{v_z'}}{\partial r} + 2g_z\beta\overline{v_z't'}$$

Here, the term $\overline{v_z'v_z'}\partial\overline{v_z}/\partial z$ due to its small contribution in the energy production is omitted. The reason for the different behavior lies in the way the shear stress ($\overline{v_r'v_z'}$) acts in case of the vertical cylinder. In none of the other two cases, does the shear stress become negative near the location of the maximum velocity as it does in case of the vertical cylinder. This creates a positive production near the location of the minimum shear stress as shown in Figure 5.5. In the other two boundary layers, since the turbulent shear stress always remains positive, the total production $P_{\overline{v_z'v_z'}}$ is negative in the region $0 < (r/r_{max})^{1/3} < 1$. At the location of maximum velocity the production term becomes zero and gradually increases as r increases.

Figure 5.6 compares the shear stress and turbulent heat fluxes of the three different boundary layers: vertical channel, vertical cylinder and

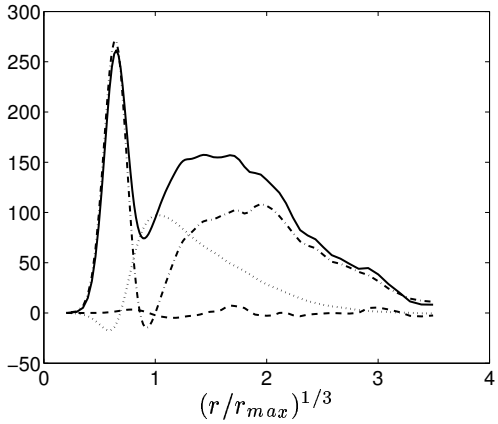

Figure 5.5: Production in the transport equation of $\overline{v_z' v_z'}$ at $Gr_z = 8.9 \cdot 10^{10}$, $z/H = 0.54$. Solid line: total production; dash-dotted line: $-2\overline{v_r' v_z'}\frac{\partial \overline{v_z'}}{\partial r}$; dashed lines: $\overline{v_z' v_z'}\partial \overline{v_z}/\partial z$; dotted lines: $2g_z\beta\overline{v_z' t'}$.

vertical flat plate. As can be seen, contrary to the vertical cylinder and the vertical flat plate, the wall-normal turbulent heat flux in the vertical channel is everywhere larger than the shear stress. Also all turbulent heat fluxes as well as the shear stress in case of vertical channel are much larger compared to those of the vertical cylinder and the flat plate. Similar to the vertical flat plate, the shear stress in vertical channel never becomes negative. Although a negative stream-wise turbulent heat flux does exist in both the vertical cylinder and the flat plate boundary layers, this region can not be seen in the vertical channel boundary layer. The study of mixed and forced convection boundary layers in a vertical channel by Davidson *et al.* (2003) also suggests that similar to the natural convection boundary layer in the vertical cylinder, the normalized wall-normal turbulent heat flux is larger than the normalized turbulent shear stress. In both cases of the forced and the mixed convection, there exist a region close to the hot wall in which the turbulent shear stress is negative. Also in both cases there exist a region in which the stream-wise turbulent heat flux is negative close to the hot wall contrary to the natural convection boundary layer in the vertical channel.

Another difference between the vertical channel flow and the other two boundary layers is in the location of the maxima of the wall-normal turbulent heat fluxes. In both cases of the vertical cylinder and the flat plate boundary layers, the locations of the turbulent heat fluxes maxima lie in the inner part of the boundary layer close to the location of the maximum velocity. However, in the vertical channel, the

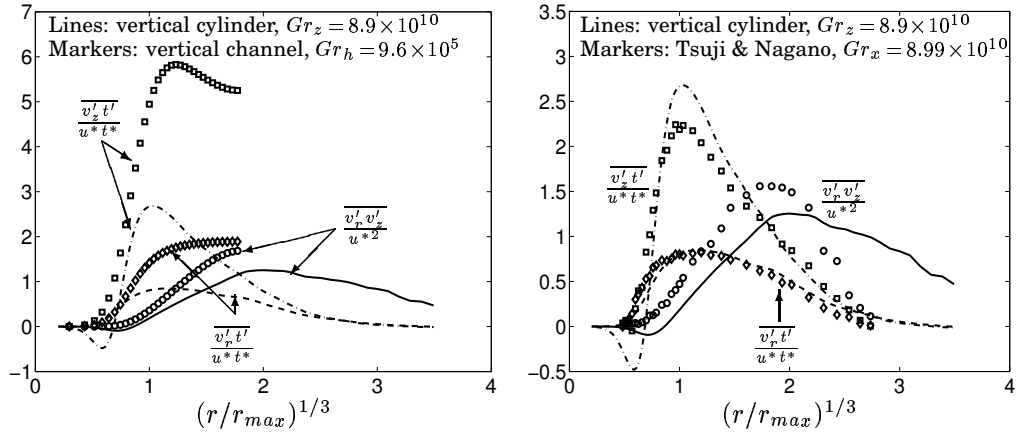

(a) (b)

Figure 5.6: Comparison of the shear stress and turbulent heat fluxes of the three different boundary layers.

wall-normal heat flux is almost constant from the location of maximum velocity to the middle of the channel. In the vertical channel, no advection is present so the wall heat flux is transported from the hot wall to the cold wall entirely by viscous and turbulent diffusion. This can be seen by integrating the temperature equation 4.3 which yields:

$$q_w = -\overline{v't'} + \frac{\nu}{Pr}\frac{\partial T}{\partial y}$$

The viscous diffusion is important only close to the wall. As q_w is constant, the wall normal turbulent heat flux remains almost constant in main part of the boundary layer in the middle of the channel (Davidson *et al.* (2003)). Nevertheless, in all cases, the maximum shear stress lies in the outer part of the boundary layer where both normal stresses are maximum.

The momentum and temperature equations can be integrated in order to study the important terms in the boundary layer. In two-dimensional form, the integral form of z-momentum and temperature equations

read:

$$v_z - Balance = -\overbrace{\int_{R_i}^{r}\left[\frac{1}{r}\frac{\partial}{\partial r}(rv_r v_z)+\frac{\partial}{\partial z}(v_z^2)\right]rdr}^{AT}+$$
$$\overbrace{\int_0^r g\beta(T-T_{ref})rdr}^{BT}+\underbrace{\int_{R_i}^{r}\left[\frac{1}{r}\frac{\partial}{\partial r}(r\nu_{eff,v}\frac{\partial v_z}{\partial r})+\frac{\partial}{\partial z}(\nu_{eff,v}\frac{\partial v_z}{\partial z})\right]rdr}_{VT}- \quad (5.1)$$
$$\underbrace{\int_{R_i}^{r}\left[\frac{1}{r}\frac{\partial}{\partial r}(r\overline{v_r' v_z'})+\frac{\partial}{\partial z}\overline{v_z' v_z'}\right]rdr}_{FT}-\underbrace{\int_{R_i}^{r}\frac{1}{\rho}\frac{\partial p}{\partial z}rdr}_{PT}$$

$$T - Balance = -\overbrace{\int_{R_i}^{r}\left[\frac{1}{r}\frac{\partial}{\partial r}(rv_r T)+\frac{\partial}{\partial z}(v_z T)\right]rdr}^{AT}+$$
$$\underbrace{\int_{R_i}^{r}\left[\frac{1}{r}\frac{\partial}{\partial r}(r\nu_{eff,T}\frac{\partial T}{\partial r})+\frac{\partial}{\partial z}(\nu_{eff,T}\frac{\partial T}{\partial z})\right]rdr}_{CT}- \quad (5.2)$$
$$\underbrace{\int_{R_i}^{r}\left[\frac{1}{r}\frac{\partial}{\partial r}(r\overline{v_r' t'})+\frac{\partial}{\partial z}\overline{v_z' t'}\right]rdr}_{FT}$$

Figure 5.7 shows the integral form of the z-momentum and the temperature equations part by part. All terms in Figures 5.7(a) and 5.7(b) are normalized with u^{*2} and $u^* t^*$, respectively, and the pressure term (PT) in Figure 5.7(a) is not included. From Figure 5.7(a) it can be found that as the maximum velocity location is approached ($r^+ = 37$), the viscous diffusion term (VT) becomes negligible. Consequently, the fluctuating term (FT), to which the shear stress mainly contributes, increases in order to balance the buoyancy term (BT) increment. The advective term (AT) is almost negligible in the entire boundary layer. Contrary to the momentum equation, there is no buoyancy term in the energy equation. So, as can be seen, the fluctuating terms here balance the conductive terms. This is one reason why the wall-normal turbulent heat flux reaches its maximum in the inner part of the boundary layer. It should be mentioned here that the contribution of the stream-wise turbulent heat flux to the fluctuating term is almost negligible.

It is almost impossible to get a completely two-dimensional result out of three-dimensional calculations unless the number of computational time steps approaches infinity. Since it is impossible to perform such

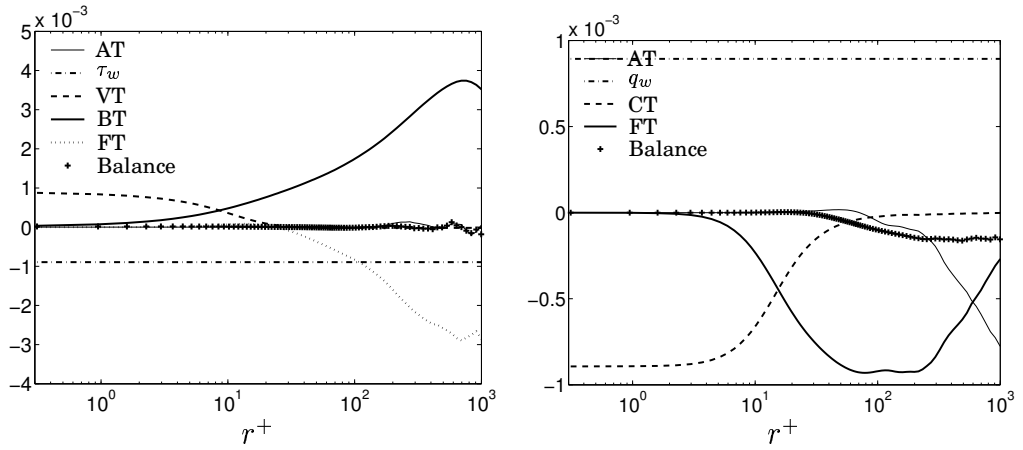

(a) v_z-equation.

(b) temperature equation.

Figure 5.7: Integral form of the z-momentum and temperature equations at $Gr_z = 8.9 \cdot 10^{10}$.

a simulation, there are always some errors in averaged parameters. This can be shown especially by plotting those variables which analytically are known to be zero. Figure 5.8 shows the normalized stresses which are supposed to become zero analytically in the LES computations. Comparing the magnitudes of $\overline{v_r' v_\theta'}$ and $\overline{v_\theta' v_z'}$ with the magnitude of turbulent shear stress in Figure 3.20 it can be found that at maximum, they get values equal to 3% and 10% of the maximum shear stress, respectively. $\overline{v_\theta' t'}$, at maximum, get a value equal to 15% of the maximum wall-normal turbulent heat flux and almost 5% of the maximum stream-wise turbulent heat flux. A part of this error comes from the way the turbulent stresses and heat fluxes are calculated. In fact, the flow governing equations are solved with the Crank-Nicolson method which is a semi-implicit method. However, the average parameters including the resolved stresses are calculated implicitly at the end of each time step. This is probably what causes the relatively large balance term in Figure 5.7(b)

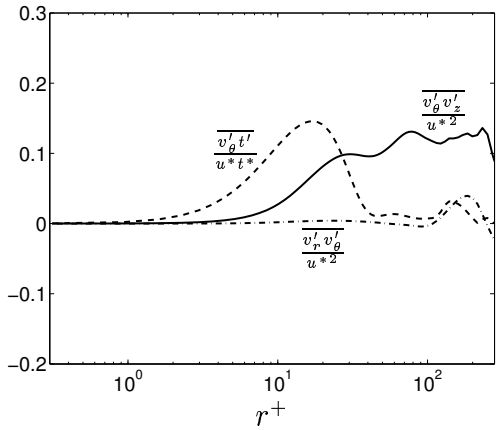

Figure 5.8: Accuracy of LES result by considering turbulent stresses which are supposed to become zero ($Gr_z = 8.9 \cdot 10^{10}$).

Bibliography

ABE, K., KONDOH, T. & NAGANO, Y. 1994 A new turbulence model for predicting fluid flow and heat transfer in separating and reattaching flows - 1. Flow field calculations. *Int. J. Heat Mass Transfer* **37**, 139–151.

BETTS, P. L. & BOKHARI, I. H. 2000 Experiments on turbulent natural convection in an enclosed tall cavity. *International Journal of Heat and Fluid Flow* **21** (6), 675–683.

BURMEISTER, L. C. 1993 *Convective Heat Transfer*. New York: John Wiley & Sons.

CHEESEWRIGHT, R. 1968 Turbulent natural convection from a plane vertical surface. *Journal of Heat Transfer* **90**, 1–8.

CHEESEWRIGHT, R. & IEROKIPIOTIS, E. 1984 Measurements in a turbulent natural convection boundary layer. In *1st UK National Conference on Heat Transfer*, , vol. 2, pp. 849–856.

CUI, A. & STREET, R. L. 2001 Large-eddy simulation of turbulent rotating convective flow development. *J. Fluid Mech.* **447**, 53–84.

DAHLSTRÖM, S. & DAVIDSON, L. 2003 Large eddy simulation applied to a high-reynolds flow around an airfoil close to stall. AIAA paper 2003-0776.

DAVIDSON, L., ČUTURIĆ, D. & PENG, S.-H. 2003 DNS in a plane vertical channel with and without buoyancy. In *Turbulence Heat and Mass Transfer 4* (ed. K. Hanjalić, Y. Nagano & M. Tummers), pp. 401–408. New York, Wallingford (UK): begell house, inc.

DAVIDSON, L. & FARHANIEH, B. 1995 CALC-BFC: A finite-volume code employing collocated variable arrangement and cartesian velocity components for computation of fluid flow and heat transfer in complex three-dimensional geometries. Rept. 95/11. Dept. of Thermo

and Fluid Dynamics, Chalmers University of Technology, Gothenburg.

DAVIDSON, L. & PENG, S.-H. 2003 Hybrid LES-RANS: A one-equation SGS model combined with a $k - \omega$ model for predicting recirculating flows. *International Journal for Numerical Methods in Fluids* **43**, 1003–1018.

EIDSON, T. M. 1985 Numerical simulation of the turbulent Rayleigh-Bénard problem using subgrid modelling. *Journal of Fluid Mechanics* **158**, 245–268.

EMVIN, P. 1997 The full multigrid method applied to turbulent flow in ventilated enclosures using structured and unstructured grids. PhD thesis, Dept. of Thermo and Fluid Dynamics, Chalmers University of Technology, Göteborg.

FERZIGER, J. H. & PERIC, M. 1996 *Computational Methods for Fluid Dynamics*. Berlin: Springer-Verlag.

FUJII, T., TAKEUCHI, M., FUJII, M., SUZAKI, K. & UEHARA, H. 1970 Experiments on natural-convection heat transfer from the outer surface of a vertical cylinder to liquids. *Int. J. Heat Mass Transfer* **13**, 753–787.

GEORGE, W. K. & CAPP, S. P. 1979 A theory for natural convection turbulent boundary layers next to heated vertical surfaces. *International Journal of Heat and Mass Transfer* **22**, 813–826.

GOLDSTEIN, R. J., ECKERT, E. R. G., IBELE, W. E., PATANKAR, S. V., SIMON, T. W., KUEHN, T. H., STRYKOWSKI, P. J., TAMMA, K. K., BAR-COHEN, A., HEBERLEIN, J. V. R., DAVIDSON, J. H., BISCHOF, J., KULACKI, F. A., KORTSHAGEN, U. & GARRICK, S. 2002 Heat transfer - a review of 2000 literature. *International Journal of Heat and Mass Transfer* **45** (14), 2853–2957.

HANJALIC, K. 1994 Achievements and limitations in modelling and computation of buoyant turbulent flows and heat transfer. In *10th Int. Heat Transfer Conference*. Brighton, UK.

IIDA, O. & KASAGI, N. 1997 Direct numerical simulation of unstably stratified turbulent channel flow. *Journal of Heat Transfer* **119**, 53–61.

KALTENBACH, H. J., FATICA, M., MITTAL, R., LUND, T. S. & MOIN, P. 1999 Study of flow in a planar asymmetric diffuser using large-eddy simulation. *Journal of Fluid Mechanics* **390**, 151–185.

KASAGI, N. & IIDA, O. 1999 Progress in direct numerical simulation of turbulent heat transfer. In *ASME/JSME Joint Thermal Engineering Conference*. San Diego, California.

KITAMURA, K., KOIKE, M., FUKUOKA, I. & SAITO, T. 1985 Large eddy structure and heat transfer of turbulent natural convection along a vertical flat plate. *Int. J. Heat Mass Transfer* **28**, 837–850.

KOTSOVINOS, N. E. 1991 Turbulence spectra in free convection flow. *Physics of Fluids A* **3** (1), 163–167.

KUTATELADZE, S. S., KIRDYASHKIN, A. G. & IVAKIN, V. P. 1972 Turbulent natural convection on a vertical plate and in a vertical layer. *Int. J. Heat Mass Transfer* **15**, 193–202.

LOCK, G. S. H. & TROTTER, F. J. D. 1968 Observations on the structure of a turbulent free convection boundary layer. *Int. J. Heat Mass Transfer* **11**, 1225–1232.

MARY, I. & SAGAUT, P. 2002 Large eddy simulation of flow around an airfoil near stall. *AIAA Journal* **40** (6), 1139–1145.

MIKI, Y., FUKUDA, K. & TANIGUCHI, N. 1993 Large eddy simulation of turbulent natural convection in concentric horizontal annuli. *Int. J. Heat and Fluid Flow* **14**, 210–216.

MILLER, D. S. 1990 *Internal Flow Systems*. British Hydraulic Research Association.

MIYAMOTO, M., KAJINO, H., KURIMA, J. & TAKANAMI, I. 1982 Development of turbulence characteristics in a vertical free convection boundary layer. In *7th Int. Heat Transfer Conference*, , vol. 2, pp. 323–328. Munich.

NA, Y. & HANRATTY, T. J. 2000 Limiting behavior of turbulent scalar transport colse to a wall. *International Journal of Heat and Mass Transfer* **43**, 1749–1758.

NIEUWSTADT, F. T. M. & VERSTEEGH, T. A. M. 1997 Dns of natural convection between two vertical,differentially heated walls. In *Proc. 11th Symp. on Turbulent Shear Flows*. Grenoble.

NINGYU, L., XIYUN, L. & LIXIAN, Z. 2000 A dynamic subgrid-scale model for the large eddy simulation of stratified flow. *Science in China* **43** (4), 391–399.

OSTRACH, S. 1952 An analysis of laminar free-convection flow and heat transfer about a plate parallel to the direction of the generating body force. Report 1111. NACA.

PENG, S.-H. & DAVIDSON, L. 1998 Comparison of subgrid-scale models in LES for turbulent convection flow with heat transfer. In *2nd EF Conference in Turbulent Heat Transfer*, , vol. 1, pp. 5.24–5.35. Manchester.

PENG, S.-H. & DAVIDSON, L. 1999 Computation of turbulent buoyant flows in enclosures with LRN $k-\omega$ models. *International Journal of Heat and Fluid Flow* **20**, 172–184.

PENG, S.-H. & DAVIDSON, L. 2001*a* Comparative study of LES for turbulent buoyant flow in terms of SGS model and grid resolution. In *The Second International Symp. on Turbulence and Shear Flow Phenomena* (ed. E. Lindborg, A. Johansson, J. Eaton, J. Humphrey, N. Kasagi, M. Leschziner & M. Sommerfeld), , vol. 2, pp. 455–460. Stockholm.

PENG, S.-H. & DAVIDSON, L. 2001*b* Large eddy simulation for turbulent buoyant flow in a confined cavity. *International Journal of Heat and Fluid Flow* **22**, 323–331.

PENG, S.-H. & DAVIDSON, L. 2002 On a subgrid-scale heat flux model for large eddy simulation of turbulent thermal flow. *International Journal of Heat and Mass Transfer* **45**, 1393–1405.

PENG, S.-H., DAVIDSON, L. & HOLMBERG, S. 1997 A modified low-Reynolds-number $k-\omega$ model for recirculating flows. *ASME: Journal of Fluids Engineering* **119**, 867–875.

PERSSON, N. J. & KARLSSON, R. I. 1996 Turbulent natural convection around a heated vertical slender cylinder. In *8th Int. Symp. on Applications of Laser Techniques to Fluid Mechanics*. Lisbon.

POPE, S. B. 2000 *Turbulent Flows*. Cambridge, United Kingdom: Cambridge University Press.

SOHANKAR, A., NORBERG, C. & DAVIDSON, L. 1998 Low-Reynolds number flow around a square cylinder at incidence: Study of blockage, onset of vortex shedding and outlet boundary condition. *International Journal for Numerical Methods in Fluids* **26**, 39–56.

TIAN, Y. S. & KARAYIANNIS, T. G. 2000*a* Low turbulence natural convection in an air filled square cavity part i: the thermal and fluid flow fields. *International Journal of Heat and Mass Transfer* **43**, 849–866.

TIAN, Y. S. & KARAYIANNIS, T. G. 2000*b* Low turbulence natural convection in an air filled square cavity part ii: the turbulence quantities. *International Journal of Heat and Mass Transfer* **43**, 867–884.

TIESZEN, S., OOI, A., DURBIN, P. & BEHNIA, M. 1998 Modeling of natural convection heat transfer. pp. 287–302. Proceedings of the summer program: Center for turbulence research.

TSUJI, T. & NAGANO, Y. 1988*a* Characteristics of a turbulent natural convection boundary layer along a vertical flat plate. *International Journal of Heat and Mass Transfer* **31** (8), 1723–1734.

TSUJI, T. & NAGANO, Y. 1988*b* Turbulence measurements in a natural convection boundary layer along a vertical flat plate. *International Journal of Heat and Mass Transfer* **31** (10), 2101–2111.

VERSTEEGH, H. K. & MALALASEKERA, W. 1995 *An Introduction to Computational Fluid Dynamics - The Finite Volume Method*. Harlow, England: Longman Scientific & Technical.

VERSTEEGH, T. A. M. & NIEUWSTADT, F. T. M. 1998 Turbulent budgets of natural convection in an infinite, differentially heated, vertical channel. *International Journal of Heat and Fluid Flow* **19**, 135–149.

VLIET, G. C. & LIU, C. K. 1969 An experimental study of turbulent natural convection boundary layers. *Journal of Heat Transfer* **91**, 517–531.

WARNER, C. Y. & ARPACI, V. S. 1968 An experimental investigation of turbulent natural convection in air at low pressure along a vertival heated flat plate. *Int. J. Heat Mass Transfer* **11**, 397–406.

WOSNIK, M. & GEORGE, W. K. 1995 Another look at the turbulent natural convection boundary layer next to heated vertical surfaces. In *ICHMT Symposium on Turbulence, Heat and Mass Transfer*. Lisbon.

ZHANG, W. & CHEN, Q. 2000 Large eddy simulation of indoor airflow with a filtered dynamic subgrid scale model. *International Journal of Heat and Mass Transfer* **43**, 3219–3231.

Appendix A

Energy Spectrum Calculation

Assume that $f(x)$, $-\infty < x < \infty$, is piece-wise differentiable and absolutely integrable. The Fourier transform of the function $f(x)$ is defined as:

$$F(k) = \hat{f}(k) = \frac{1}{2\pi} \int_{-\infty}^{\infty} f(x) e^{-ikx} dx \tag{A.1}$$

Suppose that $\{f(x_n)\}_{n=1..N}$ is a set of N-periodic complex-valued data for which:

$$f(x_1) = f(x_{N+1})$$

The discrete Fourier transform or DFT of this set of data is defined as:

$$F(k_m) = \hat{f}(k_m) = \sum_{n=1}^{N} f(x_n) e^{-2\pi i (m-1)(n-1)/N}, \qquad \text{for } m = 1..N \tag{A.2}$$

To calculate the discrete Fourier transform of a set of data, many mathematical operations are needed. Hence, the computation of a large set of data can be very time consuming. Fast Fourier transform or FFT is an algorithm which reduces the number of operations for DFT if $N = 2^i$ in which i is a natural number. The FFT algorithm is a built-in function in most of the mathematical packages such as MATLAB™. However, these packages design the FFT functions in a general way in order to be useful in all kind of applications. For the purpose of energy spectrum,

the FFT in MATLAB™should be modified. Considering Equation A.1, the FFT estimation of it is computed as follows:

$$\begin{aligned}
\hat{f}(k) &= \frac{1}{2\pi}\int_{-\infty}^{\infty} f(x)e^{-ikx}dx \\
\hat{f}(k_m) &= \frac{1}{2\pi}\sum_{n=1}^{N} f(x_n)e^{-i[\frac{2\pi}{L}(m-1)][(n-1)\Delta x]}\Delta x \\
&= \frac{1}{2\pi}\Delta x\sum_{n=1}^{N} f(x_n)e^{-i[\frac{2\pi}{L}(m-1)][(n-1)\frac{L}{N}]} \\
&= \frac{\Delta x}{2\pi}\sum_{n=1}^{N} f(x_n)e^{-2\pi i(m-1)(n-1)/N} \\
&= \frac{\Delta x}{2\pi}FFT(f(x_n)), \quad m = 1..N, \quad k_m = \frac{2\pi}{L}(m-1)
\end{aligned}$$

In the present work, as the cyclic boundary condition is the θ direction, the energy spectra of the spatial two-point correlations at radius R are calculated as follows (Note that the energy spectrum is defined as the *twice* of the Fourier transform of the two-point correlation function):

$$\begin{aligned}
E_{ij}(\kappa_m) &= 2\cdot\frac{R\Delta\theta}{2\pi}\sum_{n=1}^{N} R_{ij}(n)e^{-2\pi i(m-1)(n-1)/N} \\
&= \frac{R\Delta\theta}{\pi}FFT(R_{ij}(n))
\end{aligned} \tag{A.3}$$

In which:

$$\begin{cases}
m = 1..N \\
\kappa_m = 2\pi(m-1)/(R\cdot\theta_{\mathit{eff}}) \\
\Delta\theta = \theta_{max}/(n_k-1) \\
\theta_{\mathit{eff}} = N\Delta\theta
\end{cases}$$

n_k is the number of nodes in the θ-direction. For the present LES results, $n_k = 162$ and $\theta_{max} = \pi/2$. It should be mentioned that in the present work $N = n_k - 2 = 160$. The reason is that since cyclic boundary condition is applied in the θ-direction, the 1^{st} node is the same as $(n_k-1)^{th}$ node and the 2^{nd} node is the same as n_k^{th} node. This means that the effective span-wise extension is in fact $(n_k-2)\Delta\theta$. Also

$R_{ij}(n_k - 1) = R_{ij}(1)$ showing that $N + 1 = n_k - 1$ or $N = n_k - 2$. This is shown in Figure A.1.

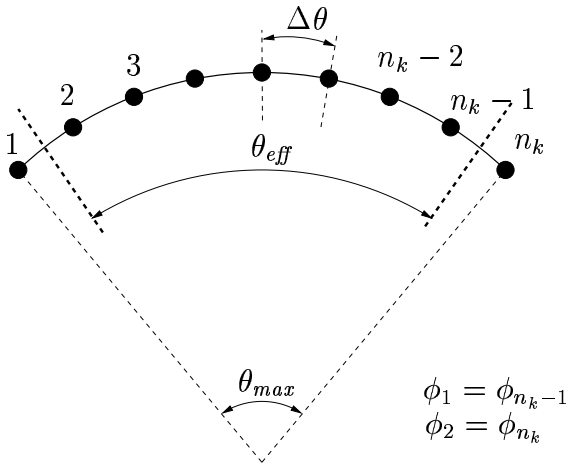

Figure A.1: Schematic diagram of a grid with cyclic boundary conditions in θ direction.